Communications Biology

https://doi.org/10.1038/s42003-026-09929-9

Article in Press

Single-stranded DNA in the bone microenvironment promotes prostate cancer bone metastasis via the ITGA6-FAK pathway

Received: 16 April 2025

Accepted: 16 March 2026

Cite this article as: Chen, X., Ye, M.-s., Peng, Z.-L. *et al.* Single-stranded DNA in the bone microenvironment promotes prostate cancer bone metastasis via the ITGA6-FAK pathway. *Commun Biol* (2026). https://doi.org/10.1038/s42003-026-09929-9

Xin Chen, Ming-sheng Ye, Zhuo-Lin Peng, Feng Yan, Yuan Xiao, Yu-jue Li & Ye Xiao

Single-stranded DNA in the bone microenvironment promotes prostate cancer bone metastasis via the ITGA6-FAK pathway

Xin Chen[1,2], Ming-sheng Ye[1], Zhuo-Lin Peng[1], Feng Yan[3], Yuan Xiao[1,2*], Yu-jue Li[1,2*], Ye Xiao[1,2*]

1 Department of Endocrinology, Endocrinology Research Center, Xiangya Hospital of Central South University, Changsha, China
2 National Clinical Research Center for Geriatric Disease, Xiangya Hospital, Changsha, China
3 Hunan Nanhua Biotechnology Co., Ltd, Changsha, China
*Corresponding author. Tel: +86 0731 89752728; Fax: +86 0731 84327332;
E-mail: 18163837229@163.com (Yu-jue Li); annie.yuan@163.com (Yuan Xiao); xiaoye@csu.edu.cn (Ye Xiao)
*These authors jointly supervised this work

Abstract

Bone metastases represent a critical phenotype of prostate cancer progression, driven by factors within the bone microenvironment. However, the molecular mechanisms underlying this progression remain poorly understood. In this study, we observed a significant accumulation of single-stranded DNA within the metastatic bone microenvironment of PCa patients. Through cell-SELEX methodology, we identified a PCa target-specific ssDNA, EHBP1. Specifically, EHBP1-ssDNA specifically captures PCa cells by binding to the transmembrane protein integrin α6, which subsequently activates the integrin α6-FAK signaling pathway. Functional studies revealed that knockdown of integrin-α6 expression effectively abrogated EHBP1-ssDNA mediated PCa bone metastatic capacity. Notably, these findings were recapitulated through pharmacological inhibition of FAK signaling using Defactinib, an FAK-specific inhibitor. Taken together, our findings reveal that bone-marrow ssDNA may represent a bone microenvironment factor that captures and promotes PCa homing to bone, further suggesting a potential therapeutic strategy for mitigating bone metastasis.

Key Words

Prostate cancer, bone metastases, single-stranded DNA, integrin α6, FAK

Introduction

Prostate cancer (PCa) is the second most commonly diagnosed cancer in men and one of the leading cancer types for the estimated new cancer deaths (1, 2). Although the overall incidence of PCa has decreased due to the advent of PET/CT imaging techniques and early detection of metastatic disease, the proportion of patients diagnosed with bone metastatic disease at the time of diagnosis has risen over the past decade (3, 4). Clinically, anti-androgen therapies remain the clinical standard of care for advanced PCa. However, despite initial therapeutic responses, a substantial proportion of patients with advanced PCa will ultimately progress to castration-resistant prostate cancer despite continued anti-androgen treatment (5, 6). By further elucidating the cellular and molecular mechanisms underlying bone metastasis in prostate cancer, we may facilitate the development of targeted therapies. Such advancements hold significant promise for improving clinical outcomes and enhancing the survival rates of patients with metastatic disease.

Emerging evidence has established that alterations within the primary tumor microenvironment represent a critical determinant driving PCa progression and metastatic colonization. These modifications, originating from genetic aberrations and modulated by non-epithelial stromal components - including cancer-associated fibroblasts, tumor-infiltrating immune cells, and endothelial cells - create a permissive niche that facilitates PCa cell growth, invasion, and dissemination (7). Certain PCa cells, having acquired migratory capabilities, will enter the blood or lymphatic circulation by decreasing their adhesion to the cells and extracellular matrix (ECM) of tumor microenvironment, and subsequently home to secondary organs, particularly bone and brain. Prior to progression, the primary tumor remotely triggers a pathological remodeling of bone tissue by releasing extracellular vesicles or signaling molecules (such as interleukins, vascular endothelial growth factors (VEGFs), and TGF-β), thereby establishing a "pre-metastatic niche" in secondary organs (8, 9). These have entered circulating malignant tumor cells over-expressing ligands such as integrins β1, α4β1, and α5β1, cadherin-11, connective tissue growth factor, and CXCR4 interact with receptor proteins present in the bone marrow stroma, including the urokinase receptor, vascular cell adhesion molecule-1, and fibronectin. This interaction facilitates their homing to the bone marrow (10-12). These findings indicate that the biological and molecular remodeling of the bone microenvironment is attributed to the preferential metastasis of tumor cells to bone. Certainly, a deeper understanding of the intricate interactions within the tumor-bone microenvironment and the involvement of multiple signaling pathways in its progression will facilitate the development of potent strategies to inhibit the disease progression.

Bone marrow supernatant fluid (BMSF), a specialized biopsy fluid, may function as a reservoir for growth factors that orchestrate tumor bone metastasis, notably TGF-β, bone morphogenetic proteins, insulin-like growth factor, VEGF, and platelet-derived growth factor (13, 14). Recent studies have demonstrated the existence of Versican-associated cell-free microRNAs within BMSF, suggesting that this biopsy fluid also harbors nucleic acid fragments (15). So far, however, it remains unclear whether BMSF contains other nucleic acids, such as extracellular DNA. According to previous studies, extracellular DNA (exDNA) was indeed detected in various bodily fluids, where it enters circulation following cell death-whether as part of normal physiological cell turnover or pathological processes (16). These exDNA constitutes a complex heterogeneous mixture of short DNA fragments, encompassing conventional double-stranded linear segments alongside alternative topological structures such as circular and single-stranded conformations (17). For example, research report that plasma contains ultrashort single-stranded DNA in addition to nucleosomal cell-free DNA by ultra-short cell-free DNA sequencing (18). The observation was independently confirmed by another study group (19). Previously researches report that exDNA is relatively short (18), with a length of approximately 50 nucleotides. These short, single-stranded DNA or RNA molecules can be generated through Systematic Evolution of Ligands by Exponential Enrichment (SELEX) that bind to specific molecular targets with high affinity(20). It is known that both bone matrix and bone marrow undergo continuous and dynamic turnover processes (21), strongly suggesting that this process contributes to the formation of exDNA in BMSF. Hence, in this study, we hypothesize that BMSF harbors abnormally generated single-stranded DNA (ssDNA), which may serve to capture circulating PCa cells entering the bone microenvironment and facilitate their adhesion to bone tissues.

In the present study, we discovered that BMSFs derived from PCa patients with bone metastases were enriched in ssDNA. Furthermore, through a cell-SELEX strategy, we identified a high-affinity ssDNA specific to prostate cancer cells, EHBP1-ssDNA. Additionally, we identified ITGA6 as a binding target for EHBP1-ssDNA. The binding of EHBP1-ssDNA to ITGA6 substantially enhances the adhesion and proliferation of PC-

3 cells via the integrin α6-FAK pathway, the effect that was reversed upon treatment with Defactinib. Our work presents a theory explaining the preferential skeletal localization of PCa and offers a promising strategy for PCa bone metastasis treatment.

Method

Clinical Samples

Clinical samples were collected from Xiangya Hospital, Central South University, in accordance with the Declaration of Helsinki. The study was approved by the Ethics Committee of Xiangya Hospital (Approval No. 2024081279), and written informed consent was obtained from all participants. All ethical regulations relevant to human research participants were followed.

Serum samples were obtained from 20 treatment-naïve patients with prostate bone metastasis and 20 non-cancer controls (n=20 per group). Bone marrow supernatants were collected from a subset of 3 patients per group with traumatic fractures (n=3 per group).

All enrolled patients met the inclusion criteria (metastasis group: histologically confirmed, untreated prostate cancer with bone metastasis; control group: no cancer, undergoing fracture surgery). Randomization was not applicable, as patients were allocated based on disease status. To minimize potential confounders, all samples were processed in a blinded manner and in random order within each batch. No samples were excluded due to quality issues or missing data; thus, all 20 serum samples per group and 3 bone marrow supernatants per subgroup were included in the final analyses. To ensure strict adherence to ethical standards, bone marrow samples from controls were derived exclusively from surgical waste tissue generated during routine procedures; no additional or unnecessary biopsies were performed on healthy individuals.

Mice

Six weeks old male wild-type BALB/c nude mice were purchased from Beijing Vital River Laboratory Animal Technology Co., Ltd., and bred and maintained by Hunan SJA Laboratory Animal Company (China). All animal work was performed in strict accordance with all relevant ethical regulations for animal use and was approved by the Animal Ethics Committee at Hunan SJA Laboratory Animal Company (IACUC-SJA2023110).

A total of 80 mice were used in this study. Mice were randomly assigned to experimental groups using a random number table. To minimize confounding factors: (i) surgeries and treatments were performed in an alternating order between groups; (ii) bioluminescence imaging (BLI) measurements were conducted at consistent times of day and in randomized cage order; (iii) investigators performing outcome assessments were blinded to group allocation.

All animals completed the study, and no exclusions were made; therefore, data from all 80 mice were included in the final analyses. In each experiment, mice were randomly assigned to experimental groups as described below, with 8 mice per group: Experiment for Figure 1: Group 1 (vehicle + scrambled DNA, n=8) and Group 2 (scrambled DNA + ssDNA, n=8). Experiment for Figure 3: sgControl group (n=8), sgITGA6 group (n=8), sgControl + EHBP1-ssDNA group (n=8) and sgITGA6 + EHBP1-ssDNA group (n=8). Experiment for Figure 5: Vehicle group (n=8), Defactinib group (n=8), Vehicle + EHBP1-ssDNA group (n=8) and Defactinib + EHBP1-ssDNA group (n=8).

Sample size (n=8 per group) was determined a priori by power analysis based on pilot data (primary outcome: BLI signal), which indicated that 7 mice per group were sufficient to achieve 80% power at α=0.05. We increased

this to 8 to account for potential technical variability, while adhering to the 3Rs principles. We have complied with all relevant ethical regulations for animal use.

Cell culture

Human prostate cancer cell line C4-2B (ZQ1110) and Luciferase-expressing prostate cancer cell line (PC-3-luc, LZQ0024) was purchased from Shanghai Zhong Qiao Xin Zhou Biotechnology Co., Ltd. The human breast cancer cell lines ZR-75-1 (CL-0247), MDA-MB-231 (CL-0150), and MCF-7 (CL-0149), as well as the non-tumorigenic human prostate epithelial cell line RWPE-1 (catalog no. CL-0200), were purchased from Wuhan Pricella Biotechnology Co., Ltd. C4-2B, PC-3-luc, and RWPE-1 were derived from male donors; ZR-75-1, MDA-MB-231, and MCF-7 from female donors. None of these cell lines appear in the ICLAC Register of Misidentified Cell Lines (version 13, http://iclac.org/databases/cross-contaminations).

Cell lines were not re-authenticated by the authors but were certified mycoplasma-negative by suppliers prior to distribution using standardized PCR-based methods. C4-2B and PC-3-luc cells were cultured in Ham's F12 medium (Gibco) supplemented with 10% fetal bovine serum (FBS; Sigma-Aldrich) and 1% penicillin/streptomycin (P/S; Solarbio). ZR-75-1 cells were maintained in RPMI-1640 medium (Gibco) supplemented with 10% FBS (Sigma-Aldrich) and 1% P/S (Solarbio). MDA-MB-231 and MCF-7 cells were grown in DMEM (Gibco) containing 10% FBS and 1% P/S. RWPE-1 cells were cultured in the specific culture medium for RWPE-1 cells (Pricella, CM-0200). All cells were incubated at 37°C in a humidified atmosphere containing 5% CO_2.

Tumor implantation and bioluminescence analysis

For the intra-cardiac injection model, $1x10^6$ PC-3-luc cells were injected into the left cardiac ventricle of anesthetized mice. The maximum tumor burden permitted by the ethics committee was defined as: (1) primary tumor volume not exceeding 1,800 mm^3; (2) metastatic burden causing less than 18% body weight loss; (3) absence of ulceration, necrosis, or signs of distress. Throughout the experimental period, all animals were monitored daily for signs of distress, body weight changes, and overall health condition. The maximal tumor size/burden permitted by the ethics committee was not exceeded in any animal in this study. Animals were euthanized immediately if they exhibited signs of severe distress, rapid weight loss (>18% of initial body weight), neurological deficits, or hind limb paralysis.

The development of metastases was monitored by BLI. In vivo bioluminescence imaging was performed weekly with IVIS Spectrum (PerkinElmer). Anesthetized mice were intraperitoneally injected with 100μl of 15 mg/kg D-Luciferin (Invitrogen, L2912). Analysis was performed with Living Image software (PerkinElmer), and all images were normalized to the same radiance scale. Average radiance intensity was quantified in units of radiance ($p\ s^{-1}\ cm^{-2}\ sr^{-1}$). In order to quantify luminescence in specific areas of the mice, regions of interest (ROIs) were drawn around right leg.

Adhesion, migration and invasion assays

The adhesion assay was performed using 96-multi well plates coated with 10μg/ml fibronectin (Solarbio, F8180). Cells were seeded inside wells containing culture media without serum. After 24 hours, cells that adhered to the bottom of the wells were fixed in 4% formaldehyde. The fixed cells were stained using 0.1% crystal violet (Solarbio, G1063). The assay was quantified by counting the stained nuclei in 5 independent fields of five

repeated wells.

Assays of migration and invasion were performed using 6.5-mm transwell inserts (Corning, 3422) coated with nothing or growth-factor-reduced Matrigel (Corning, 354230), respectively. Cells were serum-starved overnight before seeding to eliminate the interference of proliferative effect with cell migration or invasion. Cells were seeded inside transwell inserts containing culture media without serum. After 16 hours, cells that translocated to the lower surface of filters were fixed in 4% formaldehyde. The fixed membranes were stained using 0.1% crystal violet. Assays were quantified by counting the stained nuclei in 5 independent fields of five repeated transwells.

Colony formation assay

To evaluate the proliferation capability, a colony formation assay was performed. Complete medium mentioned in the cell culture method section above, containing 10 nM of candidate ssDNA, Scrambled DNA, or maintained under conditions for ITGA6 knockdown or not (transfection with sgRNA), was applied to PC-3 cells. Subsequently, the pre-treated cells were harvested and seeded into 12-well plates at a density of 200 cells per well. The cells were cultured in complete medium containing the respective treatments at 37°C for 10 days to allow colony formation. The culture medium was refreshed every 3 days. After incubation, the colonies were washed with PBS, fixed with 4% paraformaldehyde for 20 min, and stained with 0.1% crystal violet solution for 10 min.

Hydroxyapatite chromatography

Human bone marrows were collected and were subjected to centrifugation to separate the BMSF. BMSF was injected into a clean centrifuge tube, filtered through a 100-um cell filter, and centrifuged at 1200 r/min for 5 min. The supernatant was collected. The DNA from the supernatant was then extracted through treatment with the MagMAX DNA Multi-Sample Ultra 2.0 Kit (Thermo Scientific, A36570). Combine DNA with 0.12M phosphate buffer in a final volume of 500 μl and incubate at 60°C for 10 minutes. Allow the DNA to bind to the illustra NAP-5 Columns (Cytiva, 17085301) for 30 minutes. Open the stopcock and collect the initial ssDNA sample in the 15ml tube. Add 6ml of 0.12M phosphate buffer to the columns, and collect single-stranded DNA in the same tube. Add 1 volume of phenol: chloroform: isoamyl alcohol (25:25:1 v/v/v) solution to the tube, mix vigorously, and centrifuge at 3500 g for 15 minutes. Transfer supernatant containing ssDNA to a new 15ml tube. Desalt collected ssDNA samples with an Amicon Ultra-4 centrifugal filter device outfitted with a 30,000 molecular weight cut-off Ultracel membrane (Merck, UFC803024). Schematics were created with BioGDP.com(22) and MedPeer (www.medpeer.cn).

Cell-SELEX selection

The initial DNA library was generated from ssDNA isolated from bone marrow supernatant fluid of prostate cancer patients with bone metastasis, following the protocol (ABclonal RK20222) and dissolved in binding buffer (0.01 M pH 7.4 PBS containing 5 mM $MgCl_2$, 0.2 mg/mL tRNA, 1 mg/mL salmon sperm DNA, 2 mg/mL BSA) (23, 24). After denaturation at 95 °C for 5 min and immediate cooling on ice for 10 min, the initial library was incubated for 2 h with PC-3 cells cultured at 90% confluence in 100 mm dishes at 4 °C. After incubation, the supernatant was removed and the cells were washed with washing buffer. PC-3 cells were then harvested and transferred to 500 μL of water and heated for 10 min at 95 °C to collect cell-bound DNA. FAM-labelled forward

primers and biotin-labelled reverse primers were prepared by PCR using cell-bound DNA as a template (6-14 cycles of 30 s at 95 °C, 30 s at 58 °C, 30 s at 72 °C, and then 30 s at 72 °C for 5 min). The double-stranded DNA (dsDNA) product was then separated from the PCR solution by streptavidin-coated agarose beads (GE Healthcare). After treatment with 0.2 M NaOH, FAM-labelled ssDNA was separated from dsDNA, desalted and lyophilized for the next round of selection. Starting from the third round, the evolved ssDNA pool was first incubated with RWPE-1 cells in 60 mm Petri dishes at 90% confluence for 30 min at 4°C for subtractive selection. Unbound ssDNA was then removed and applied to PC-3 cells. To increase the stringency of selection, the positive incubation time was shortened from 2 h to 1 h and the washing time was gradually extended from two to three times as the number of selection rounds increased. Meanwhile, the negative incubation time was gradually increased from 1 h to 2 h. Starting from the 9th round of selection, two consecutive subtractive selections were carried out to maximize the removal of ssDNA bound to normal prostate cells. The ssDNA library derived from the 12th round of iterative selection underwent PCR amplification, followed by cloning into a T-vector system and subsequent Sanger sequencing (services provided by Sangon Biotech Co., Ltd.). The name of ssDNAs were based on their respective corresponding gene names. The "EHBP1-ssDNA," for instance, is so named because its sequence maps specifically to the EHBP1 gene.

Flow Cytometry Analysis

To evaluate the binding ability of candidate ssDNA to cells, flow cytometry was performed. In brief, PC-3 cells (2×10^5cells) was incubated with 250 nM candidate FAM-labelled ssDNA or FAM-labelled libraries in 250 μL of binding buffer for 1 h at 4°C. The cells were then washed three times with washing buffer and resuspended in 200 μL of D-PBS for analysis.

To determine the dissociation constant (Kd), a saturation binding assay was conducted, and PC-3 cells (3×10^5) were incubated with different concentrations (0, 20, 50, 100 and 200 nM) of ssDNA in 250 μL of binding buffer for 1 h at 4°C. After incubation, each sample was washed three times with washing buffer and then resuspended in 200 μL D-PBS for flow cytometry analysis. These experiments were repeated three times. Using GraphPad Prism 9.5 software, the Kd of ssDNA was calculated by Equation Y as Bmax * X/(Kd + X) (Y: relative fluorescence intensity; X: ssDNA concentration), fitting the dependence of the fluorescence intensity of the cell/ssDNA complexes on the ssDNA concentration.

Micro-CT analysis and histochemistry of mouse femur

The fresh femurs were dissected and fixed in 4% paraformaldehyde for 24 hours. The fixed samples were scanned using high-resolution micro-CT (Skyscan 1172, Bruker micro-CT) following a previously described method(25). After micro-CT analysis, the femurs were decalcified in 10% EDTA for 2 weeks, embedded in paraffin, and cut to 4 μm. As described previously, the 4-μm paraffin sections were stained with hematoxylin-eosin (26).

Cyto-immunofluorescent staining

PC-3 cells were cultured for 24 hours and fixed in 4% paraformaldehyde for 20 minutes. Then cells were permeabilized with 0.25% Triton X-100 (Sigma-Aldrich, T8787) for 20 minutes, and incubated with primary antibodies against ITGA6 (R&D Systems, MAB13501, 1:100) and ITGB4 (Santa Cruz Biotechnology, sc-

514426, 1:50), followed by incubation with secondary antibodies. Nuclei were counterstained with DAPI (Beyotime, C1006). The fluorescent signals were captured via fluorescence microscopy (Apotome 3, Zeiss).

Western blotting

Western blotting was performed as described previously(27). Blots were incubated with primary antibodies described as the following: FAK (Forevertech Biotechnologies Co., Ltd, 20431, 1:1000), p-FAK (Tyr397) (CST, 3283S, 1:1000), AKT (CST, 9272S, 1:1000), p-AKT (CST, 4060S, 1:1000), ERK (CTS, 9102S, 1:1000), p-ERK (CST, 4370S, 1:1000), ITGA6 (proteintech, 27189-1-AP, 1:1000), ITGB4 (proteintech, 21738-1-AP, 1:1000), and GAPDH (Origene, TA802519, 1:5000). Secondary antibodies including Goat anti-Mouse IgG (H+L) Secondary Antibody, HRP (Invitrogen, AB_228307) and Goat anti-Rabbit IgG (H+L) Secondary Antibody, HRP (Invitrogen, AB-228341) were subsequently applied.

Immunoprecipitation (IP)

Briefly, PC-3 cells were lysed in the cell lysis buffer (Beyotime, P0013D) with protease inhibitor (Selleck, B14001) for 10 minutes on ice, and then centrifuged at 13, 000 × g for 5 minutes. The supernatants were collected and incubated overnight at 4°C with ~5 μg ITGA6 or IgG antibody and Protein A/G magnetic beads (MCE, HY-K0202). After washing for four times with IP buffer, Magnetic Beads were boiled with 2× SDS loading buffer followed by Western blotting using ITGA6 (proteintech, 27189-1-AP, 1:1000) and FAK (Forevertech Biotechnologies Co., Ltd, 20431, 1:1000).

Biotin pull-down assay

We got ssDNA labeled with biotin from Sangon Biotech (Shanghai)Co.,Ltd. PC-3 cells were lysed in the cell lysis buffer (Beyotime, P0013D) with protease inhibitor (Selleck, B14001) for 10 minutes on ice, and then centrifuged at 13, 000 × g for 5 minutes. To perform the binding assay, biotin-labeled ssDNA was incubated with the supernatant ad Protein A/G magnetic beads (MCE, HY-K0202) overnight at 4°C. Non-labeled ssDNA was used as a negative control. After washing for four times with IP buffer, magnetic beads were boiled with 2× SDS loading buffer followed by Western blotting using ITGA6 (proteintech, 27189-1-AP, 1:1000) and ITGB4 (proteintech, 21738-1-AP, 1:1000)

ssDNA treatment

Scrambled ssDNA sequence with a length of 80 bp and EHBP1-ssDNA were synthesized by Sangon Biotech(Shanghai)Co.,Ltd. For the injection of either a scrambled ssDNA sequence or EHBP1-ssDNA, intra-bone marrow delivery was performed following a previously described method (28). The scrambled ssDNA and EHBP1-ssDNA were diluted with sterile 1×PBS to a final concentration of 50 nM. Fifty microliters of each solution were injected into the bone marrow cavity of the right femur twice weekly for one month.

ssDNA Binding Assay

PC-3 cells (1×10^4 cells), including a control cell line and an ITGA6 knockdown cell line, were seeded into 24-well cell culture plates and cultured in F12 medium supplemented with 10% fetal bovine serum (FBS) and 1% penicillin/streptomycin (P/S). One hour prior to the assay, the culture medium was replaced with fresh medium containing 1 mg/mL salmon sperm DNA and 0.2 mg/mL tRNA, and the cells were incubated at 37 °C for one

hour. EHBP1-ssDNA sequences with FAM modification and a control scrambled sequence with a length of 80 bp were denatured at 70 °C for 3 minutes and then allowed to refold at room temperature for 20 minutes. These refolded ssDNA sequences were added to the seeded cells in full growth medium and incubated at 37 °C for 1 hour unless otherwise specified. One hour later, the cell supernatant was removed and cells were washed three times with 1×PBS. Images were captured using an inverted fluorescent microscope (Ti2-A, Nikon).

Mass spectrometry analysis

For mass spectrometry analysis, the protein isolated via both biotin pull-down and His-tag pull-down assays was subjected to enzymatic digestion, desalting, concentration, and final reconstitution. Each sample was labeled using TMT reagent (Thermo Scientific). LC-MS/MS analysis was performed as described(29).

RNA isolation and qRT-PCR analysis

RNA isolation and qRT-PCR analysis was performed as described previously(30). The primer sequences were listed as follows: GAPDH: Forward- 5'-GGAGCGAGATCCCTCCAAAAT-3', Reverse-5'-GGCTGTTGTCATACTTCTCATGG-3'; ITGA6 Forward- 5'-TGGCGTGGCTGACTT ACAT-3', Reverse-5'-TGGCGTGGCTGACTTACAT-3'; ITGB4: Forward- 5'-CCAGGAAGAUCC AUUUCAATT-3', Reverse -5'-UUGAAAUGGAUCUUCCUGGTT-3'.

Defactinib treatment

Defactinib (MedChemExpress, 1073154-85-4) at 25 mg/kg was administered via oral gavage once a day for 4 weeks. Control mice received vehicle only. The EHBP1-ssDNA was injected into the bone marrow cavity of the right femur twice a month for 1 month.

Statistics and Reproducibility

Statistical analyses were performed with GraphPad Prism 9.5. The data are presented as mean ± SEM. Comparisons between two experimental groups were assessed using unpaired two-tailed Student's t-tests. For comparisons involving three or more groups, one-way analysis of variance (ANOVA) with Tukey's post hoc test was applied. Survival differences were evaluated using the two-sided log-rank test. $P<0.05$ was used to define statistical significance and indicated by '*'; $P < 0.05$ were indicated by '**'; $P < 0.01$ were indicated by '***'; $P < 0.001$ were indicated by '****'.

Sample sizes were determined based on power calculations from pilot studies and established precedents in comparable preclinical models. In vivo experiments utilized eight mice per experimental group ($n = 8$), representing biological replicates. Human sample analyses included bone marrow supernatants from three non-cancer bone fracture patients (control) and bone metastasis patients (sample sizes detailed in figure legends), and serum samples from twenty non-cancer individuals and bone metastasis patients. For in vitro studies, experiments were independently repeated at least three times (as specified: $n = 3$ or $n = 5$ independent experiments), with each independent experiment constituting a separate biological replicate performed on different days. Technical replicates (e.g., triplicate wells in binding or functional assays) were averaged for each independent experiment. All representative images and quantitative data presented are derived from these independent replicates, confirming the reproducibility of the results.

Results

ssDNA associates with bone metastases in prostate cancer

To determine whether bone marrow supernatant fluid contains ssDNA, we collected bone marrow samples from three PCa patients with bone metastasis and concomitant bone fracture, as well as three normal bone marrow samples from Xiangya Hospita. Total nucleic acid was extracted from BMSF and then loaded onto hydroxyapatite chromatography for the isolation of ssDNA (Figure 1A). We successfully isolated ssDNA from bone marrow samples and observed that it has an length of about 80 bps (Figure 1B). Furthermore, the ssDNA concentration in the bone microenvironment and serum was significantly higher in patients with bone metastases (met) compared to those non-cancer fracture samples (normal), as quantified by gel electrophoresis and concentration assays (Figure 1C-1D). The result suggest an association between elevated ssDNA levels and the presence of bone metastasis, potentially reflecting increased cell turnover/damage in advanced cancers. Additionally, it raises the possibility that ssDNA may contribute to the remodeling of the bone microenvironment. Thus, we put forward this finding as a hypothesis-generating observation, warranting further mechanistic investigation.

To further investigate whether BMSF ssDNA is involved in the progression of bone metastasis in PCa, we inoculated PC-3-luc cells into the left ventricles of nude mice to establish systemic bone metastases. Subsequently, we locally injected BMSF ssDNA into the femurs as follows: in Group 1, vehicle was delivered to the left femur and scrambled DNA into the right femur; in Group 2, scrambled DNA was injected into the left femur and ssDNA into the right femur (Figure 1E). Bioluminescence images were captured weekly, and images at 4th week were used for analysis. We found that there was no difference between femurs treated with scrambled DNA and vehicle, while there was significantly greater tumor area burden in femurs injected with ssDNA compared to scrambled DNA (Figure 1F-1G). Survival analysis revealed significantly reduced longevity in the group 2 compared to group 1 (Figure 1H). Post-euthanasia analysis demonstrated concordant results between imaging and histological assessments: ssDNA-injected bones exhibited marked bone deterioration through micro-CT quantification, showing reduced trabecular bone volume (BV/TV) and decreased trabecular thickness (Tb.Th) (Figure 1I-1J) and displayed larger tumor volumes by H&E staining (Figure 1K-1L). These findings demonstrate that ssDNA, derived from the BMSF of PCa patients, possesses the ability to enhance bone metastasis in PCa.

EHBP1-ssDNA promotes prostate cancer bone metastasis by binding to integrin α6.

Based on our findings, the ssDNA isolated from the BMSF of PCa patients is approximately 80 nucleotides in lenth, which we hypothesized to exhibit high affinity specifically for prostate cancer. Using PC-3 cells, a bone metastasis-derived standard model for prostate cancer studies(31, 32), as targets and normal RWPE-1 prostate cells for counter-selection, we conducted 12 rounds of cell-SELEX with patient-derived ssDNA directly as the initial library (Figure 2A). Deep sequencing identified three predominant ssDNA by Round 12, among which ssDNA EHBP1 exhibited superior binding affinity to PC-3 cells as demonstrated by flow cytometry (Figure 2B-2C). Quantitative affinity assessment using FAM-labeled EHBP1-ssDNA showed concentration-dependent binding (Figure 2D) to PC-3 cells, a human prostate cancer cell line (Figure 2E), indicating the high - affinity interaction of EHBP1 - ssDNA with metastatic prostate cancer cells (Figure 2D). Short, single-stranded DNA or RNA oligonucleotides, such as aptamers, can bind to target molecules with high specificity and affinity (6, 24, 33). By modulating the downstream signaling pathways of their target proteins, these oligonucleotides trigger

cascade reactions at both cellular and molecular levels, ultimately inducing functional alterations in biological systems (34). To identify the target molecule for EHBP1-ssDNA, we synthesized biotin-labeled EHBP1-ssDNA and incubated it with membrane proteins from PC-3, C4-2B (prostate cancer) and MDA-MB-231 cells (a highly metastatic triple-negative breast cancer line)(35) as malignant controls, contrasting with RWPE-1 (non-tumorigenic prostate) cells and ZR-75-1 (non-metastatic ER^+ breast cancer)(36, 37) as isogenic controls. Comparative membrane proteome analysis identified proteins pulled down by biotin-modified EHBP1-ssDNA, among which ITGA6 and PLP2 exhibited high affinity and specific expression in bone metastatic cell lines (PC-3, C4-2B and MDA-MB-231) compared to non-metastatic cell lines (RWPE-1 and ZR-75-1) (Figure 2F-2G). Among them, ITGA6, a metastasis-associated adhesion receptor, is recognized for its heterodimerization with ITGB4 to form the integrin α6β4 complex, which regulates kinase signaling pathways in prostate cancer (38, 39).

Therefore, following subsequent research, we focused on the EHBP1-ssDNA target molecule, ITGA6. Using DiI, a cell membrane dye, we performed fluorescence colocalization studies which showed that ITGA6 colocalizes with DiI staining, indicating that ITGA6 was specially expressed in the cell membrane of PC-3 cells (Figure 2H). RT-qPCR analysis demonstrated that the expression levels of ITGA6 were highest in PC-3 cells when compared to other cell lines (Figure 2I). Biotin-conjugated EHBP1-ssDNA pull-down assays with magnetic beads followed by immunoblotting demonstrated direct physical interaction between EHBP1-ssDNA and both ITGA6/ITGB4 subunits (Figure 2J). Additionally, genetic silencing of ITGA6 using sgRNA in PC-3 cells significantly attenuated EHBP1-ssDNA binding (Figure 2K), and reduced the adhesion capacity induced by EHBP1-ssDNA treatment (Figure 2L-2M). These findings indicate that EHBP1-ssDNA not only effectively captures PCa cells but also promotes their proliferative activity, confirming integrin α6 as its functional receptor.

EHBP1-ssDNA facilitates PCa bone metastasis via integrin α6

To examine whether EHBP1-ssDNA facilitates prostate cancer bone metastasis through ITGA6 modulation in vivo, PC-3-luc cells were transduced with sgITGA6 or sgControl lentiviral particles to establish stable ITGA6-knockdown cell lines utilizing the CRISPR-Cas9 genome editing system. The stable ITGA6-knockdown and control cell lines were inoculated into the left ventricles of nude mice. Bioluminescence images were captured weekly, and images at 4th week were used for analysis. Compared to vehicle-treated controls, sgITGA6 group presented diminished bone metastatic foci (Figures 3A-3B), improved survival outcomes (Figures 3C), and enhanced trabecular bone preservation as demonstrated by micro-CT analysis (Figure 3D-3E).

We repeated left ventricles injection of ITGA6-knockdown and control PC-3-luc cells, and further injected EHBP1 ssDNA into the bone marrow cavity of the right leg in mice, to determine whether ITGA6 is required for EHBP1-ssDNA function. Similarly, the knockdown of ITGA6 was observed to modestly diminish EHBP1-ssDNA' s pro-metastatic activity in the sgITGA6+EHBP1-ssDNA treatment group, indicated by bioluminescence (Figure 3F-3G), survival analysis (Figure 3H), micro-CT (Figure 3I-3J), and H&E staining (Figure 3K-3L), as compared to the sgControl+EHBP1-ssDNA group. Collectively, these findings demonstrate that EHBP1-ssDNA facilitates prostate cancer metastasis through interaction with the ITGA6 receptor, whereas ITGA6 knockdown partially counteracts EHBP1-ssDNA' s pro-metastatic activity.

EHBP1-ssDNA activates the integrin α6-FAK signaling pathway in PCa.

In order to identify the downstream proteins involved in the oncogenic pathways mediated by EHBP1-

ssDNA/ITGA6, we performed His-tagged ITGA6 pull-down assays using total membrane proteins from PC-3 cells, followed by LC-MS/MS proteomic profiling. This approach robustly identified focal adhesion kinase (FAK) as a high-confidence interacting partner of ITGA6 (Figure 4A-4B). Critically, co-immunoprecipitation experiments confirmed a direct physical interaction between endogenous ITGA6 and FAK in PC-3 cells (Figure 4C), establishing a molecular link between this integrin and a master regulator of cancer progression. It is well established that the activation of FAK/AKT and FAK/ERK signaling pathways is vital for cancer progression(40, 41). Notably, EHBP1-ssDNA treatment induced robust, dose- and time-dependent phosphorylation of FAK at Tyr397, an activation marker in PC-3 cells(42), concomitant with downstream AKT and ERK activation (Figure 4D-4G), key effectors in tumor survival and migration.

To determine whether EHBP1-ssDNA activates the FAK pathway through ITGA6-mediated mechanisms, we cultured both ITGA6-knockdown and control PC-3-luc cells, treated them with EHBP1-ssDNA or scrambled DNA, then analyzed FAK/AKT/ERK activation by western blotting. Strikingly, genetic knockdown of ITGA6 completely abolished EHBP1-ssDNA-induced phosphorylation of FAK, AKT, and ERK (Figure 4H-I), demonstrating that ITGA6 is essential for transducing EHBP1-ssDNA signals into FAK pathway activation. To further validate our findings, Defactinib, a FAK-specific inhibitor targeting Tyr397 phosphorylation (43), was employed to pharmacologically inhibit FAK signaling. Consistent with the results observed in ITGA6 knockdown cells, Defactinib treatment similarly abrogated EHBP1-ssDNA-induced FAK/AKT/ERK activation (Figure 4J-4K), and significantly attenuated EHBP1-ssDNA enhanced cell adhesion, invasion, and migration in vitro (Figure 4L-4M). Together, we suggested that EHBP1-ssDNA drives metastatic signaling through integrin α6β4-FAK axis, with FAK phosphorylation serving as a critical mechanistic hub for downstream oncogenic pathway activation.

FAK inhibitor Defactinib attenuates the EHBP1-ssDNA' s pro-bone metastatic capacity

Notably, the results showed that Defactinib not only suppressed baseline FAK/AKT and FAK/ERK signaling but alomost reversed EHBP1-ssDNA-induced FAK activation and pro-metastatic effects (Figure 4J-4K), highlighting FAK's therapeutic potential and prompting in vivo validation. For in vivo validation, PC-3-luc cells were inoculated into the left ventricles of nude mice. Following this, the mice were treated with Defactinib or control vehicle. Bioluminescence revealed that Defactinib significantly reduced the bone metastasis signals (Figure 5A), and was associated with improved survival outcomes (Figure 5B). To further evaluate the therapeutic effect, we repeated the experiment in a parallel cohort of mice in which EHBP1-ssDNA was injected into the right femur. Consistently, Defactinib treatment modestly attenuated the pro-metastatic effect of EHBP1-ssDNA, as evidenced by reduced bioluminescence signals (Figure 5C-5D).

Micro-CT analysis demonstrated that Defactinib preserved bone architecture in both experimental settings, reflected by increased bone volume and trabecular thickness (Figure 5E-5H). Histological examination by H&E staining corroborated these findings, showing smaller tumor volumes in Defactinib-treated mice compared to vehicle controls (Figure 5I-5J). These findings suggested that Defactinib can attenuate the pro-bone metastatic effects of EHBP1-ssDNA by inhibiting FAK.

Discussion

Bone metastases are virtually incurable and result in significant morbidity prior to PCa patients' death(44, 45). Successful colonization of bone metastatic cells requires reciprocal communications with

microenvironmental cells and local cell factors. In this study, we propose a theory to explain the propensity of PCa for bone metastasis. Specifically, we demonstrate that ssDNA present in BMSF exhibits properties capable of: (1) capturing circulating PCa cells as they enter the bone microenvironment, and (2) mediating their adhesion to bone tissues.

Some oligonucleotides can interact with the surface structure of target proteins through specific secondary or tertiary structures, offering potential for modulating protein function and conformational changes(46). While oligonucleotides such as aptamers have been found to exhibit anti-tumor effects in a number of cancer types, including prostate, breast, kidney and lung cancers(47-49), few studies have mentioned their pro-tumor effects. Here, we demonstrate that BMSF ssDNA exhibits properties akin to neutrophil extracellular traps (NETs), which capture PCa cells infiltrating the bone micro-environment and promote their metastatic colonization in bone. In recent years, treatment based on DNase I, a secreted enzyme capable of degrading NET-DNA, has been applied to mitigate cancer metastasis (50, 51). Consistent with these studies, our findings suggest that targeting BMSF-derived ssDNA could represent a feasible therapeutic target to mitigate PCa bone metastasis. We showed that elevated ssDNA concentration in bone marrow supernatant strongly correlates with bone metastasis and provides a pool from which tumor-cell-binding aptamers can be enriched. Additionally, it is worth noting that ultra-short cell-free circulating DNA fragments (~50 nucleotides) in plasma exist predominantly as a single-stranded conformation, as demonstrated by ultra-short cell-free DNA sequencing (17, 18). Notably, plasma from cancer patients contains significant amounts of cell-free circulating tumor DNA, which has emerged as a promising liquid biopsy-based biomarker for noninvasive diagnosis, prognosis, and longitudinal monitoring of tumor dynamics across diverse malignancies (52, 53). This phenomenon strongly suggests that ssDNA in cancer patient plasma may play a critical role in facilitating the distant metastasis of circulating tumor cells. This will be further confirmed in our subsequent research.

The formation of ssDNA is a common feature of DNA metabolism, occurring during DNA replication, repair, and recombination (54). Notably, a specific R-loop structure frequently occurs in the process, and it consists of an RNA/DNA heteroduplex along with a looped-out non-template strand. Recent studies have indeed shown that R loops are involved in many human illnesses including cancer, neurological disorders, and autoimmune diseases (55). In our study, BMSF ssDNA and R-loop structures were mainly located at bone type-H vessels. This observation readily suggests that BMSF ssDNA may originate from the bone type-H vessels. The next question is whether and how PCa cells actively promote bone type-H vessels R-loop formation. Emerging evidence suggests that the dormant and proliferating circulating tumor cells (CTCs) are found in E-selectin and stromal cell-derived factor 1 rich perisinusoidal vascular regions (11). Based on these observations, we hypothesize that CTCs interact with bone type H vessels and trigger R-loop formation through undefined mechanisms. Elucidating these underlying regulatory pathways and the release of BMSF ssDNA will be pivotal in deciphering the intricate cross-talk between CTCs and the bone microenvironment in the future.

Integrins, a class of heterodimeric transmembrane glycoproteins, mediate cell-cell and cell-ECM adhesion while regulating cellular migration. They are widely expressed across both tumor cells and the supporting host stromal cells in the bone microenvironment. Through interactions with ECM components, integrins enable tumor cells to evade cell–cell and cell–matrix constraints, thereby facilitating invasion, migration, and metastatic colonization within new tissues and matrices (56). αβ-integrins expressed on PCa cells promote their adhesion to bone ECM proteins (e.g. collagen, fibronectin, Tenascin C), regulating cell adhesion dynamics and migratory behavior. This receptor-ligand interaction further modulates intracellular signaling cascades, thereby promoting

the recruitment of additional tumor-infiltrating cells into the evolving neoplastic microenvironment. The integrin α6β4, a specialized laminin-binding integrin, exhibits frequent overexpression across diverse cancer types, with its expression level demonstrating a strong association with both malignant progression and adverse survival outcomes in oncology patients (57-59). It significantly promotes cancer cell adhesion, migration, invasion, proliferation and tumorigenesis through activation of the Rac1, PKC, PI3K and ERK signaling pathways, which are induced through interactions with other molecules (60, 61). Our study establishes that integrin α6β4 may serve as a functional receptor for EHBP1-ssDNA, thereby implicating EHBP1-ssDNA as a pro-metastatic component of the bone microenvironment.

While FAK is a cytoplasmic non-receptor protein tyrosine kinase belonging to the protein tyrosine kinase superfamily (62, 63), our data demonstrate that microenvironmental ssDNA can trigger its activation in PCa cells through integrin α6 engagement. FAK serves as a central signaling hub that integrates inputs from specific integrins, including integrin α6, and transduces them into downstream PI3K/Akt and Ras/MAPK activation (63-65), processes that are essential for tumor cell survival, migration, and metastatic colonization of bone. The functional significance of the integrin α6-FAK axis in PCa is underscored by our experimental observations: ITGA6 knockdown abolished FAK phosphorylation (Tyr397) and downstream signaling, while Defactinib blocked EHBP1-ssDNA-induced metastasis. This dual validation confirms the pathway as non-redundant and targetable.

Clinical evidence further supports the importance of this axis: FAK overexpression and hyperactivation correlate with poor prognosis across multiple solid tumors and contribute to therapeutic resistance (66). In prostate cancer specifically, the bone metastatic niche is enriched with ssDNA fragments that can engage integrin α6 and drive FAK-dependent metastatic signaling—a mechanism that may explain the predilection of PCa for bone metastasis. Defactinib, an effective and safe oral FAK inhibitor currently being evaluated in combination therapies for pancreatic ductal adenocarcinoma (67), represents a promising therapeutic strategy for advanced prostate cancer patients with bone metastases. Our data showing that Defactinib inhibits ssDNA-enhanced metastatic behaviors provide a strong rationale for clinical evaluation of FAK inhibitors in prostate cancer, particularly in contexts where the integrin α6-FAK axis is hyperactivated.

In conclusion, we demonstrated the functional importance of EHBP1-ssDNA in bone marrow supernatant for promoting PCa metastasis to bone, mediated by activation of FAK signaling following underlying EHBP1-ssDNA-integrin α6β4 interactions. We also provide strong pre-clinical evidence for targeting EHBP1-ssDNA in the control of cancer and disrupting FAK signaling as a PCa metastasis therapy. Our study lays the foundation for the further investigation of the Defactinib as well as translational research for future clinical applications.

This study has several limitations. First, the mechanistic findings were primarily derived from mouse models and in PC-3 cell lines, validation in more animal models or even patient cohorts is needed to confirm physiological relevance. Second, while the integrin α6–FAK pathway was highlighted, the complex bone microenvironment likely involves additional factors and signaling networks that were not fully explored in this work.

Data availability

The data that support the findings of this study are available in Supplementary Data. The mass spectrometry proteomics data have been deposited to the ProteomeXchange Consortium via the PRIDE partner repository with the dataset identifier PXD074143 (Reviewer username: reviewer_pxd074143@ebi.ac.uk,

password: 71smTS4HnxaP). Unedited blot/gel images can be seen in the Supplementary Figure 1. Gating strategy of flow cytometry can be seen in Supplementary Figure 2.

Acknowledgments

This work was supported by grants from National Natural Science Foundation of China (Grant No.82471619) and Natural Science Foundation of Hunan Province (Grant No.2024JJ5459).

Author contributions

XC and YJ-L performed the major experiments and analyzed overall experimental data. YJ-L and MS-Y revised the manuscript. MS-Y and ZL-P assisted with the overall experiments and interpreted data. FY guidanced on animal experiment of left ventricular injection in mice. YX and YX designed the experiments and revised the manuscript. YX designed the experiments, curated data, acquired funding.

Competing Interests

The authors declare no competing interests

1. Siegel RL, Giaquinto AN, and Jemal A. Cancer statistics, 2024. *CA Cancer J Clin.* 2024;74(1):12-49.
2. Sung H, Ferlay J, Siegel RL, Laversanne M, Soerjomataram I, Jemal A, et al. Global Cancer Statistics 2020: GLOBOCAN Estimates of Incidence and Mortality Worldwide for 36 Cancers in 185 Countries. *CA Cancer J Clin.* 2021;71(3):209-49.
3. Berish RB, Ali AN, Telmer PG, Ronald JA, and Leong HS. Translational models of prostate cancer bone metastasis. *Nature Reviews Urology.* 2018;15(7):403-21.
4. Swami U, McFarland TR, Nussenzveig R, and Agarwal N. Advanced Prostate Cancer: Treatment Advances and Future Directions. *Trends Cancer.* 2020;6(8):702-15.
5. Ge R, Wang Z, Montironi R, Jiang Z, Cheng M, Santoni M, et al. Epigenetic modulations and lineage plasticity in advanced prostate cancer. *Ann Oncol.* 2020;31(4):470-9.
6. Lang C, Yin C, Lin K, Li Y, Yang Q, Wu Z, et al. m(6) A modification of lncRNA PCAT6 promotes bone metastasis in prostate cancer through IGF2BP2-mediated IGF1R mRNA stabilization. *Clin Transl Med.* 2021;11(6):e426.
7. Kang J, La Manna F, Bonollo F, Sampson N, Alberts IL, Mingels C, et al. Tumor microenvironment mechanisms and bone metastatic disease progression of prostate cancer. *Cancer Lett.* 2022;530:156-69.
8. Fornetti J, Welm AL, and Stewart SA. Understanding the Bone in Cancer Metastasis. *J Bone Miner Res.* 2018;33(12):2099-113.
9. Kong D, Ye C, Zhang C, Sun X, Wang F, Chen R, et al. Procoxacin bidirectionally inhibits osteoblastic and osteoclastic activity in bone and suppresses bone metastasis of prostate cancer. *J Exp Clin Cancer Res.* 2023;42(1):45.
10. Yoneda T, and Hiraga T. Crosstalk between cancer cells and bone microenvironment in bone metastasis. *Biochem Biophys Res Commun.* 2005;328(3):679-87.
11. Price TT, Burness ML, Sivan A, Warner MJ, Cheng R, Lee CH, et al. Dormant breast cancer micrometastases reside in specific bone marrow niches that regulate their transit to and from bone.

Sci Transl Med. 2016;8(340):340ra73.

12. Robinson D, Van Allen EM, Wu YM, Schultz N, Lonigro RJ, Mosquera JM, et al. Integrative clinical genomics of advanced prostate cancer. *Cell.* 2015;161(5):1215-28.
13. Zhou Q, Xie F, Zhou B, Wang J, Wu B, Li L, et al. Differentially expressed proteins identified by TMT proteomics analysis in bone marrow microenvironment of osteoporotic patients. *Osteoporos Int.* 2019;30(5):1089-98.
14. Feeley BT, Gamradt SC, Hsu WK, Liu N, Krenek L, Robbins P, et al. Influence of BMPs on the formation of osteoblastic lesions in metastatic prostate cancer. *J Bone Miner Res.* 2005;20(12):2189-99.
15. Gupta N, Kumar R, Seth T, Garg B, Sati HC, and Sharma A. Clinical significance of circulatory microRNA-203 in serum as novel potential diagnostic marker for multiple myeloma. *J Cancer Res Clin Oncol.* 2019;145(6):1601-11.
16. Rostami A, Lambie M, Yu CW, Stambolic V, Waldron JN, and Bratman SV. Senescence, Necrosis, and Apoptosis Govern Circulating Cell-free DNA Release Kinetics. *Cell Rep.* 2020;31(13):107830.
17. Lo YMD, Han DSC, Jiang P, and Chiu RWK. Epigenetics, fragmentomics, and topology of cell-free DNA in liquid biopsies. *Science.* 2021;372(6538).
18. Cheng J, Morselli M, Huang WL, Heo YJ, Pinheiro-Ferreira T, Li F, et al. Plasma contains ultrashort single-stranded DNA in addition to nucleosomal cell-free DNA. *iScience.* 2022;25(7):104554.
19. Cheng LY, Dai P, Wu LR, Patel AA, and Zhang DY. Direct capture and sequencing reveal ultra-short single-stranded DNA in biofluids. *iScience.* 2022;25(10):105046.
20. Kordasht HK, and Hasanzadeh M. Aptamer based recognition of cancer cells: Recent progress and challenges in bioanalysis. *Talanta.* 2020;220:121436.
21. Schneider A, Kalikin LM, Mattos AC, Keller ET, Allen MJ, Pienta KJ, et al. Bone turnover mediates preferential localization of prostate cancer in the skeleton. *Endocrinology.* 2005;146(4):1727-36.
22. Jiang S, Li H, Zhang L, Mu W, Zhang Y, Chen T, et al. Generic Diagramming Platform (GDP): a comprehensive database of high-quality biomedical graphics. *Nucleic Acids Res.* 2025;53(D1):D1670-d6.
23. Nakhjavani M, Giles B, Strom M, Vi C, Attenborough S, and Shigdar S. A Flow Cytometry-based Cell Surface Protein Binding Assay for Assessing Selectivity and Specificity of an Anticancer Aptamer. *J Vis Exp.* 2022(187).
24. Kelly L, Maier KE, Yan A, and Levy M. A comparative analysis of cell surface targeting aptamers. *Nature communications.* 2021;12(1):6275.
25. Li YJ, Guo Q, Ye MS, Cai G, Xiao WF, Deng S, et al. YBX1 promotes type H vessel-dependent bone formation in an m5C-dependent manner. *JCI Insight.* 2024;9(4).
26. Li CJ, Xiao Y, Sun YC, He WZ, Liu L, Huang M, et al. Senescent immune cells release grancalcin to promote skeletal aging. *Cell Metab.* 2021;33(10):1957-73.e6.
27. Xiao Y, Cai GP, Feng X, Li YJ, Guo WH, Guo Q, et al. Splicing factor YBX1 regulates bone marrow stromal cell fate during aging. *Embo j.* 2023:e111762.
28. Li CJ, Xiao Y, Yang M, Su T, Sun X, Guo Q, et al. Long noncoding RNA Bmncr regulates mesenchymal stem cell fate during skeletal aging. *J Clin Invest.* 2018;128(12):5251-66.
29. Peng H, Hu B, Xie LQ, Su T, Li CJ, Liu Y, et al. A mechanosensitive lipolytic factor in the bone marrow promotes osteogenesis and lymphopoiesis. *Cell Metab.* 2022;34(8):1168-82.e6.

30. Feng X, Wang L, Zhou R, Zhou R, Chen L, Peng H, et al. Senescent immune cells accumulation promotes brown adipose tissue dysfunction during aging. *Nature communications*. 2023;14(1):3208.
31. van Bokhoven A, Varella-Garcia M, Korch C, Johannes WU, Smith EE, Miller HL, et al. Molecular characterization of human prostate carcinoma cell lines. *Prostate.* 2003;57(3):205-25.
32. Liu CW, Peng HY, Siao AC, Tsuei YW, Lin YY, Shiah SG, et al. Resistin stimulates PC-3 prostate cancer cell growth through stimulation of SOCS3 and SOCS5 genes. *Exp Biol Med (Maywood).* 2023;248(20):1695-707.
33. Wengerter BC, Katakowski JA, Rosenberg JM, Park CG, Almo SC, Palliser D, et al. Aptamer-targeted antigen delivery. *Mol Ther.* 2014;22(7):1375-87.
34. Camorani S, Passariello M, Agnello L, Esposito S, Collina F, Cantile M, et al. Aptamer targeted therapy potentiates immune checkpoint blockade in triple-negative breast cancer. *J Exp Clin Cancer Res.* 2020;39(1):180.
35. Xu J, Ma L, Wang D, and Yang J. Uncarboxylated osteocalcin promotes proliferation and metastasis of MDA-MB-231 cells through TGF-β/SMAD3 signaling pathway. *BMC Mol Cell Biol.* 2022;23(1):18.
36. Panet F, Couture F, Kwiatkowska A, Desjardins R, Guérin B, and Day R. PACE4 is an important driver of ZR-75-1 estrogen receptor-positive breast cancer proliferation and tumor progression. *Eur J Cell Biol.* 2017;96(5):469-75.
37. Liu ZJ, Lee WJ, and Zhu BT. Selective insensitivity of ZR-75-1 human breast cancer cells to 2-methoxyestradiol: evidence for type II 17beta-hydroxysteroid dehydrogenase as the underlying cause. *Cancer Res.* 2005;65(13):5802-11.
38. de Pereda JM, Lillo MP, and Sonnenberg A. Structural basis of the interaction between integrin alpha6beta4 and plectin at the hemidesmosomes. *Embo j.* 2009;28(8):1180-90.
39. Koivusalo S, Schmidt A, Manninen A, and Wenta T. Regulation of Kinase Signaling Pathways by α6β4-Integrins and Plectin in Prostate Cancer. *Cancers (Basel).* 2022;15(1).
40. Jiang Q, Pan Y, Cheng Y, Li H, Liu D, and Li H. Lunasin suppresses the migration and invasion of breast cancer cells by inhibiting matrix metalloproteinase-2/-9 via the FAK/Akt/ERK and NF-κB signaling pathways. *Oncol Rep.* 2016;36(1):253-62.
41. Deng Z, Zeng Q, Chai J, Zhang B, Zheng W, Xu X, et al. Disintegrin Tablysin-15 Suppresses Cancer Hallmarks in Melanoma Cells by Blocking FAK/Akt/ERK and NF-κB Signaling. *Curr Cancer Drug Targets.* 2020;20(4):306-15.
42. Calalb MB, Polte TR, and Hanks SK. Tyrosine phosphorylation of focal adhesion kinase at sites in the catalytic domain regulates kinase activity: a role for Src family kinases. *Mol Cell Biol.* 1995;15(2):954-63.
43. Hu Z, Wei F, Su Y, Wang Y, Shen Y, Fang Y, et al. Histone deacetylase inhibitors promote breast cancer metastasis by elevating NEDD9 expression. *Signal Transduct Target Ther.* 2023;8(1):11.
44. Clark PE, and Torti FM. Prostate cancer and bone metastases: medical treatment. *Clin Orthop Relat Res.* 2003(415 Suppl):S148-57.
45. Clézardin P, Coleman R, Puppo M, Ottewell P, Bonnelye E, Paycha F, et al. Bone metastasis: mechanisms, therapies, and biomarkers. *Physiol Rev.* 2021;101(3):797-855.
46. Sun X, Xie L, Qiu S, Li H, Zhou Y, Zhang H, et al. Elucidation of CKAP4-remodeled cell mechanics in driving metastasis of bladder cancer through aptamer-based target discovery. *Proceedings of the*

National Academy of Sciences of the United States of America. 2022;119(16):e2110500119.

47. Bates PJ, Kahlon JB, Thomas SD, Trent JO, and Miller DM. Antiproliferative activity of G-rich oligonucleotides correlates with protein binding. *J Biol Chem.* 1999;274(37):26369-77.
48. Bates PJ, Laber DA, Miller DM, Thomas SD, and Trent JO. Discovery and development of the G-rich oligonucleotide AS1411 as a novel treatment for cancer. *Exp Mol Pathol.* 2009;86(3):151-64.
49. Dassie JP, Hernandez LI, Thomas GS, Long ME, Rockey WM, Howell CA, et al. Targeted inhibition of prostate cancer metastases with an RNA aptamer to prostate-specific membrane antigen. *Mol Ther.* 2014;22(11):1910-22.
50. Yang L, Liu Q, Zhang X, Liu X, Zhou B, Chen J, et al. DNA of neutrophil extracellular traps promotes cancer metastasis via CCDC25. *Nature.* 2020;583(7814):133-8.
51. Hawes MC, Wen F, and Elquza E. Extracellular DNA: A Bridge to Cancer. *Cancer Res.* 2015;75(20):4260-4.
52. Lin E, Hahn AW, Nussenzveig RH, Wesolowski S, Sayegh N, Maughan BL, et al. Identification of Somatic Gene Signatures in Circulating Cell-Free DNA Associated with Disease Progression in Metastatic Prostate Cancer by a Novel Machine Learning Platform. *Oncologist.* 2021;26(9):751-60.
53. Gourdin T, and Sonpavde G. Utility of cell-free nucleic acid and circulating tumor cell analyses in prostate cancer. *Asian J Androl.* 2018;20(3):230-7.
54. Ribeiro J, Abby E, Livera G, and Martini E. RPA homologs and ssDNA processing during meiotic recombination. *Chromosoma.* 2016;125(2):265-76.
55. Lam FC, Kong YW, and Yaffe MB. Inducing DNA damage through R-loops to kill cancer cells. *Mol Cell Oncol.* 2020;8(1):1848233.
56. Schneider JG, Amend SR, and Weilbaecher KN. Integrins and bone metastasis: integrating tumor cell and stromal cell interactions. *Bone.* 2011;48(1):54-65.
57. Soung YH, Gil HJ, Clifford JL, and Chung J. Role of α6β4 integrin in cell motility, invasion and metastasis of mammary tumors. *Curr Protein Pept Sci.* 2011;12(1):23-9.
58. Tagliabue E, Ghirelli C, Squicciarini P, Aiello P, Colnaghi MI, and Ménard S. Prognostic value of alpha 6 beta 4 integrin expression in breast carcinomas is affected by laminin production from tumor cells. *Clin Cancer Res.* 1998;4(2):407-10.
59. Tennenbaum T, Weiner AK, Belanger AJ, Glick AB, Hennings H, and Yuspa SH. The suprabasal expression of alpha 6 beta 4 integrin is associated with a high risk for malignant progression in mouse skin carcinogenesis. *Cancer Res.* 1993;53(20):4803-10.
60. Russell AJ, Fincher EF, Millman L, Smith R, Vela V, Waterman EA, et al. Alpha 6 beta 4 integrin regulates keratinocyte chemotaxis through differential GTPase activation and antagonism of alpha 3 beta 1 integrin. *J Cell Sci.* 2003;116(Pt 17):3543-56.
61. Shaw LM, Rabinovitz I, Wang HH, Toker A, and Mercurio AM. Activation of phosphoinositide 3-OH kinase by the alpha6beta4 integrin promotes carcinoma invasion. *Cell.* 1997;91(7):949-60.
62. Song X, Xu H, Wang P, Wang J, Affo S, Wang H, et al. Focal adhesion kinase (FAK) promotes cholangiocarcinoma development and progression via YAP activation. *J Hepatol.* 2021;75(4):888-99.
63. Jeong K, Murphy JM, Ahn EE, and Lim SS. FAK in the nucleus prevents VSMC proliferation by promoting p27 and p21 expression via Skp2 degradation. *Cardiovasc Res.* 2022;118(4):1150-63.
64. Alanko J, and Ivaska J. Endosomes: Emerging Platforms for Integrin-Mediated FAK Signalling. *Trends*

Cell Biol. 2016;26(6):391-8.

65. Alanko J, Mai A, Jacquemet G, Schauer K, Kaukonen R, Saari M, et al. Integrin endosomal signalling suppresses anoikis. *Nat Cell Biol.* 2015;17(11):1412-21.
66. Gao S, Lin BY, Yang Z, Zheng ZY, Liu ZK, Wu LM, et al. Role of overexpression of MACC1 and/or FAK in predicting prognosis of hepatocellular carcinoma after liver transplantation. *Int J Med Sci.* 2014;11(3):268-75.
67. Wang-Gillam A, Lim KH, McWilliams R, Suresh R, Lockhart AC, Brown A, et al. Defactinib, Pembrolizumab, and Gemcitabine in Patients with Advanced Treatment Refractory Pancreatic Cancer: A Phase I Dose Escalation and Expansion Study. *Clin Cancer Res.* 2022;28(24):5254-62.

Figure legends

Figure 1 Bone metastases in prostate cancer are linked with ssDNA.

A. Schematic of the workflow for extraction and analysis of ssDNA from human bone marrow supernatants.

B. Chromatogram of extracted ssDNA.

C. Representative image of agarose gel electrophoresis of ssDNA levels from bone fracture and bone metastasis patients.

D. The ssDNA concentration in bone marrow supernatants was compared between non-cancer bone fracture patients (normal, n = 3) and bone metastasis patients (met, n = 3). Meanwhile, the ssDNA concentration in serum was compared between non-cancer samples (normal, n = 20) and bone metastasis patients (met, n = 20).

E. Schematic of the experimental injection protocol. Group 1, vehicle injected into the left femur and scrambled DNA into the right femur. Group 2, scrambled DNA injected into the left femur and ssDNA into the right femur. Each group included 8 mice.

F. Representative BLI images from mice in each group (n = 8).

G. Quantification of the BLI signals measured in bone metastases from each group (n = 8).

H. Kaplan-Meier survival curve of mice from Group1 and Group2 (n = 8).

I. Representative micro-CT 3D reconstructed images from each group.

J. Quantitative Micro-CT analysis of the trabecular bone microarchitecture of femurs (n = 8).

K. Representative H&E staining of bone lesions invaded by tumors from each group. Scale bar, 100 μm.

L. Quantification of relative tumor area of mice in each group (n = 8).

*, $P < 0.05$; ***, $P < 0.001$; ****, $P < 0.0001$. Student's t-test was used for 1D, 1F, 1H and 1J. Two-sided log-rank test was used for survival difference in 1K. The error bar represent standard error of the mean. BV/TV, trabecular bone volume per tissue volume; Tb.Th, trabecular thickness. Figure 1A was created with BioGDP.com, and 1E was created with MedPeer (www.medpeer.cn).

Figure 2 EHBP1-ssDNA contributes to the bone metastasis of prostate cancer and interacts with integrin α6.

A. Schematic of cell-SELEX protocol.

B. Abundance of the top 7 sequences from cell-SELEX cycle 12.

C. The emission spectrum of FAM-conjugated candidate ssDNA binders. FAM-ssDNA was incubated with PC-3 cells at 37 °C for 30 min at a concentration of 200 nM.

D. The emission spectrum of FAM-conjugated EHBP1-ssDNA at different concentrations. FAM-EHBP1-ssDNA was incubated with PC-3 cells at 37 °C for 30 min at a series of concentrations.

E. Determination of the equilibrium dissociation constant via concentration-dependent binding of EHBP1-ssDNA to PC-3 cells (0-200 nM). Kd was calculated via GraphPad Prism program 9.5 (n = 3 for each concentration).

F. Venn diagram illustrating the overlap of membrane proteins identified by biotin-EHBP1-ssDNA pull-down assays in C4-2B, PC-3, MDA-MB-231, RWPE-1, and ZR-75-1 cell lines.

G. Mass spectrogram of the ITGA6 protein tandem mass spectrum.

H. Representative images of co-localization of ITGA6 (green), Dil (red) and DPAI (blue) immunostaining in PC-3 cells. Scale bar, 25 μm.

I. RT-qPCR analysis of ITGA6 and ITGB4 expression levels in PC-3, MDA-MB-231, RWPE-1, and ZR-75-1cells. n = 3 independent experiments.
J. Western blot analysis of the interaction between biotin-EHBP1-ssDNA and ITGA6/ITGB4.
K. Representative fluorescence images of EHBP1-ssDNA-FAM or FAM-labeled scrambled DNA sequence binding to sgControl and ITGA6-knockdown PC-3 cell lines. Corresponding bright-field images confirm cell presence. Scale bar, 50 μm.
L. Quantitative analysis of FAM fluorescence in sgControl and ITGA6-knockdown PC-3 cell lines treated with EHBP1-ssDNA-FAM or FAM-labeled scrambled DNA (n = 5).
M. Representative images of cell adhesion and colony formation. Scale bar, 100 μm.
N. Quantitative analysis of cell adhesion and colony formation. n = 5 independent experiments.
n.s., not significant; *, P<0.05; **, P < 0.01; ***, P < 0.001; ****, P < 0.0001 by one-way ANOVA with Tukey's post hoc test for multiple comparisons. The error bar represent standard error of the mean. Figure 2A was created with MedPeer (www.medpeer.cn).

Figure 3 ITGA6 knockdown suppresses bone metastasis in mice
A. Schematic of injection protocol and representative BLI images from mice in sgControl and sgITGA6 groups.
B. Quantification of the BLI signals of bone metastases in sgControl and sgITGA6 groups (n =8).
C. Kaplan-Meier survival curve of mice from sgControl and sgITGA6 groups (n = 8).
D. Representative micro-CT 3D reconstructed images from mice in sgControl and sgITGA6 groups.
E. Quantitative micro-CT analysis of the trabecular bone microarchitecture from the femurs of mice in sgControl and sgITGA6 groups (n =8).
F. Schematic of injection protocol and representative BLI images from mice in sgControl + EHBP1-ssDNA and sgITGA6 + EHBP1-ssDNA groups.
G. Quantification of the BLI signals of bone metastases in sgControl + EHBP1-ssDNA and sgITGA6 + EHBP1-ssDNA groups (n =8).
H. Kaplan-Meier survival curve of mice from sgControl + EHBP1-ssDNA and sgITGA6 + EHBP1-ssDNA groups (n = 8).
I. Representative micro-CT 3D reconstructed images from mice in sgControl + EHBP1-ssDNA and sgITGA6 + EHBP1-ssDNA groups.
J. Quantitative micro-CT analysis of the trabecular bone microarchitecture from the femurs of mice in sgControl and sgITGA6 groups (n =8).
K. Representative H&E images and quantification of bone lesions invaded by tumors from sgControl and sgITGA6 groups (n = 8). Scale bar, 100 μm.
L. Representative H&E images and quantification of bone lesions invaded by tumors from sgControl + EHBP1-ssDNA and sgITGA6 + EHBP1-ssDNA groups (n = 8). Scale bar, 100 μm.
*, P<0.05; **, P < 0.01; ***, P < 0.001; ****, P < 0.0001. Student's t-test was used for 3B, 3E, 3G, 3J, 3K and 3L. Two-sided log-rank test was used for survival difference in 3C and 3H. The error bar represent standard error of the mean. BV/TV, trabecular bone volume per tissue volume; Tb.Th, trabecular thickness. Figure 3A and 3F were created with MedPeer (www.medpeer.cn).

Figure 4 Integrin α6β4-FAK signaling pathway is activated by EHBP1-ssDNA in PCa.

A. Schematic of ITGA6 pull-down assay and LC-MS/MS analysis.
B. Mass spectrogram of the FAK protein tandem mass spectrum.
C. Co-immunoprecipitation (co-IP) analysis of the interaction between FAK and ITGA6 with or without EHBP1-ssDNA treatment.
performed using antibody to pull down in extracted proteins from PC-3 cells.
D and E. Western blotting analysis (D) of ITGA6, ITGB4, p-FAK(Try397), p-AKT, p-ERK, FAK, AKT, and ERK protein levels in PC-3 cells treated with different concentrations of EHBP1-ssDNA for 4 h, and quantification from 3 independent experiments (E). GAPDH was used as a loading control.
F and G. Western blotting analysis (F) of ITGA6, ITGB4, p-FAK(Try397), p-AKT, p-ERK, FAK, AKT, and ERK protein levels in PC-3 cells treated with 10nM EHBP1-ssDNA for different time, and quantification from 3 independent experiments (G). GAPDH was used as a loading control.
H and I. Western blotting analysis (H) of p-FAK(Try397), p-AKT, p-ERK, FAK, AKT, and ERK protein levels in sgControl or sgITGA6 transfected PC-3 cells treated with scrambled DNA or EHBP1-ssDNA or blank control, and quantification from 3 independent experiments (I). GAPDH was used as a loading control.
J and K. Western blotting analysis (J) of p-FAK(Y397), p-AKT, p-ERK, FAK, AKT, and ERK protein levels in PC-3 cells treated with or without EHBP1-ssDNA or Defactinib, and quantification from 3 independent experiments (K). GAPDH was used as a loading control.
L. Representative images of cell adhesion (top), invasion (middle), and migration (bottom) from scrambled DNA, EHBP1-ssDNA, Defactinib + scrambled DNA, Defactinib + EHBP1-ssDNA groups. Scale bar, 100 μm.
M. Quantitative analysis of cell adhesion, invasion, and migration from each group. n = 5 independent experiments.
*, P<0.05; **, P < 0.01; ***, P < 0.001; ****, P < 0.0001 by one-way ANOVA with Tukey's post hoc test. The error bar represent standard error of the mean.

Figure 5 Defactinib functions as a FAK inhibitor and blocks bone metastasis in vivo
A. Representative BLI images from mice in Vehicle and Defactinib groups.
B. Kaplan-Meier survival curve of mice in Vehicle, Defactinib, Vehicle + EHBP1-ssDNA and Defactinib + EHBP1-ssDNA groups (n = 8).
C. Representative BLI images from mice in Vehicle + EHBP1-ssDNA and Defactinib + EHBP1-ssDNA groups.
D. Quantification of the BLI signals of bone metastases in each group (n =8).
E. Representative micro-CT 3D reconstructed images from mice in Vehicle and Defactinib groups.
F. Quantitative micro-CT analysis of the trabecular bone microarchitecture of mice femurs from Vehicle and Defactinib groups (n =8).
G. Representative micro-CT 3D reconstructed images from mice in Vehicle + EHBP1-ssDNA and Defactinib + EHBP1-ssDNA groups.
H. Quantitative micro-CT analysis of the trabecular bone microarchitecture of mice femurs from Vehicle + EHBP1-ssDNA and Defactinib + EHBP1-ssDNA groups (n =8).
I. Representative H&E images and quantification of relative tumor area from mice in Vehicle and Defactinib groups (n = 8). Scale bars represent 100 μm.
J. Representative H&E images and quantification of relative tumor area from mice in Vehicle + EHBP1-ssDNA and Defactinib + EHBP1-ssDNA groups (n = 8). Scale bars represent 100 μm.

*, P<0.05; **, P < 0.01; ***, P < 0.001; ****, P < 0.0001. Student's t-test was used for 5D, 5F, 5H, 5I and 5J. Two-sided log-rank test was used for survival difference in 5B. The error bar represent standard error of the mean. BV/TV, trabecular bone volume per tissue volume; Tb.Th, trabecular thickness.

Editorial Summary:

Bone marrow ssDNA, specifically EHBP1-ssDNA, drives prostate cancer bone metastasis via integrin α6-FAK signaling, and Defactinib blocks this pathway.

Peer Review Information:

Communications Biology thanks Brian Thomas, Raffaella Gallo and the other, anonymous, reviewer(s) for their contribution to the peer review of this work. Primary Handling Editor: Johannes Stortz. A peer review file is available.

Figure 1

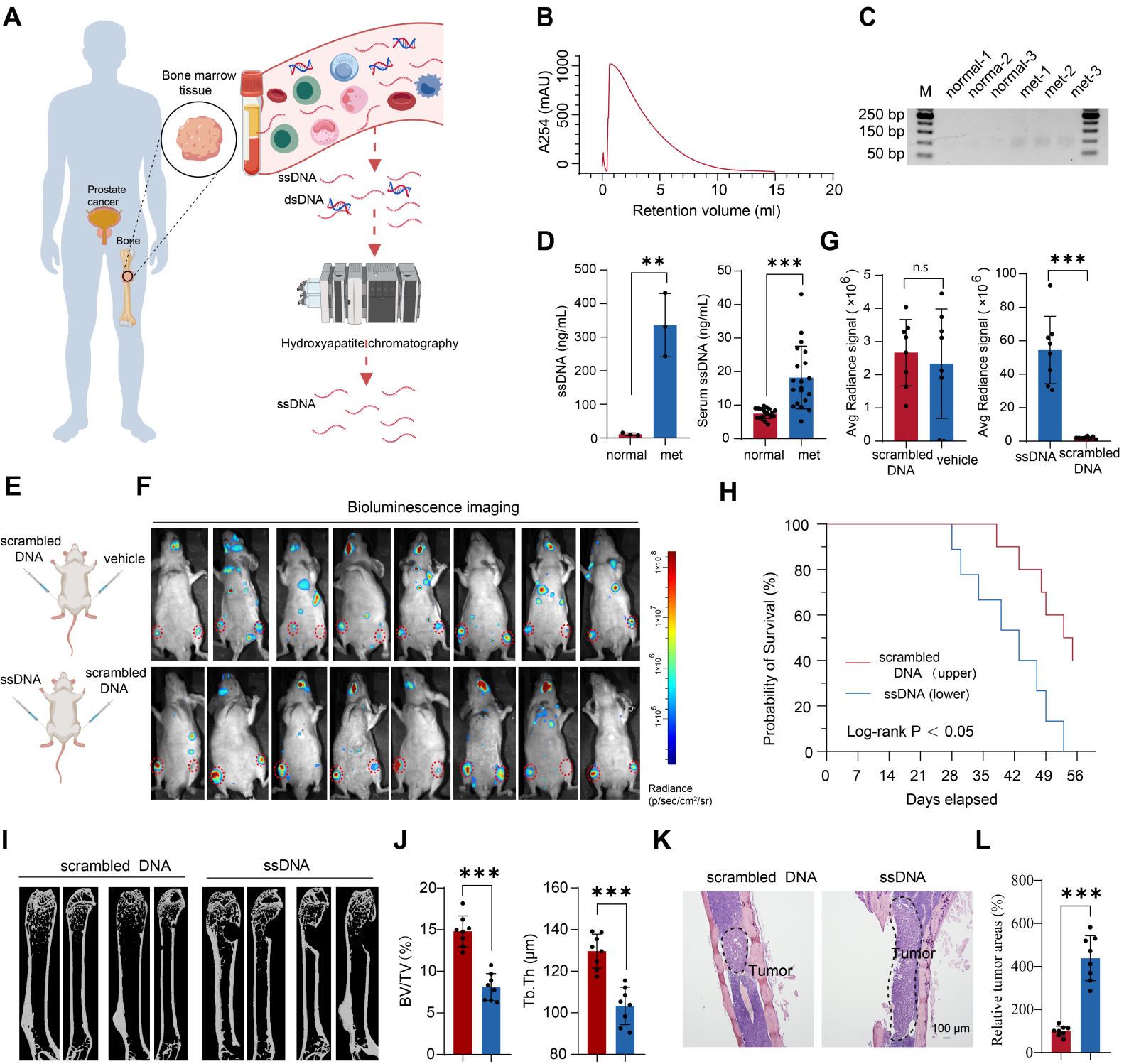
A
Bone marrow tissue
Prostate cancer
Bone
ssDNA
dsDNA
Hydroxyapatite chromatography
ssDNA
B
A254 (mAU)
Retention volume (ml)
C
M
normal-1
norma-2
normal-3
met-1
met-2
met-3
250 bp
150 bp
50 bp
D
ssDNA (ng/mL)
Serum ssDNA (ng/mL)
normal
met
G
Avg Radiance signal (×10^6)
n.s
scrambled DNA
vehicle
ssDNA
E
scrambled DNA
vehicle
ssDNA
scrambled DNA
F
Bioluminescence imaging
Radiance (p/sec/cm²/sr)
H
Probability of Survival (%)
scrambled DNA (upper)
ssDNA (lower)
Log-rank P < 0.05
Days elapsed
I
scrambled DNA
ssDNA
J
BV/TV (%)
Tb.Th (μm)
K
scrambled DNA
ssDNA
Tumor
100 μm
L
Relative tumor areas (%)

Figure 2

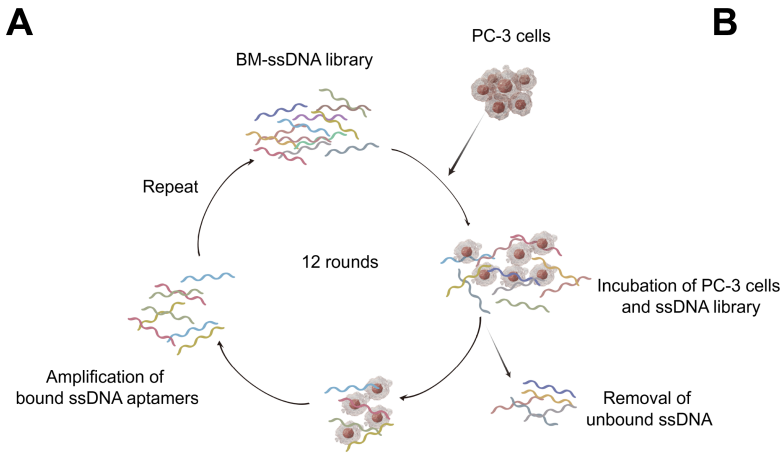

B

Name	Frequency	5'-sequence-3'
EHBP1	34/100	CTGGTGTGTGTAAGGATTTGGCATACACACATCATAACAACAAAGAAAGGTATCATAATGTACGATTCGAGAATAGCAAGG
RP11-904 M10	28/100	CATTCTATGGGTTTTGACAAATGCATGACATATATCTACCATTACAGTGCTGTAAAGAATAGGTTCATTGCCCTAAAAATCTC
CHM13	10/100	CAGTATATAATCTATATTTGATGTACTTTCATATTTTATGTACCTAATATATATTTGATGTAATTTCATATTTTATGTACAGTATAT
CLCN3	7/100	AAGTACAAAAAATTACATATATGTTAAAATTTTTTAAAAGCAACAGTATATCCAATTTCACCTCTCGATTTCATCTTACGCAT
SLC4A10	3/100	CAGGGCAGTGTGATTTCTCCAAATGAAAGAGGAACCATAACAGATTTCGTTAACAGTTTTCAATTAATAAGATCCTGTATAA
ENSA	2/100	CATGAATTCACTACCCGCCTGGGCAATATGTTGAAACCCCGTCTCTACAACAACAAAAAATAGTTTGCTAAATGTTTCCTCC
LRBA	2/100	TTTATCTTTGTGAGACTAGTGACAGGTCTGTGTAGCTTTTCTGTTCTCACTTGGGAATAGCAAATGCCTTAATGTAAAAAGT

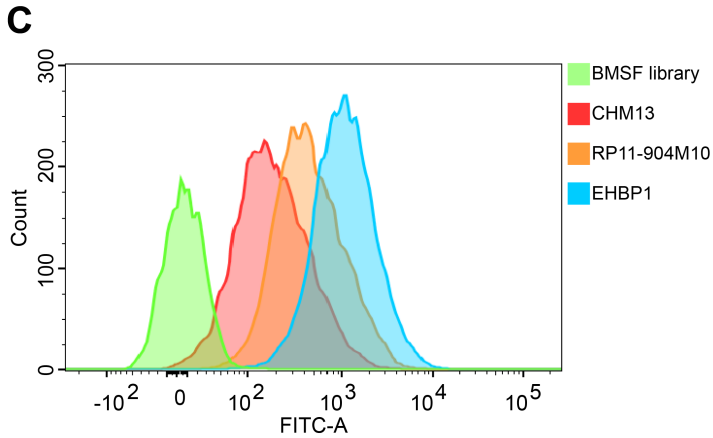

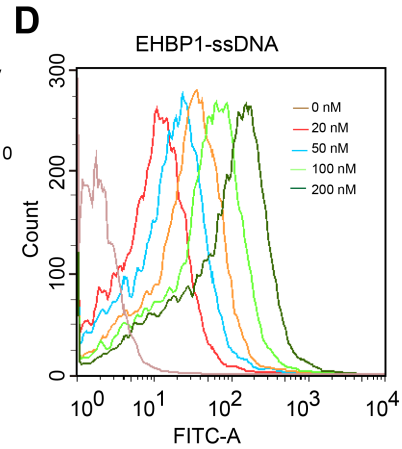

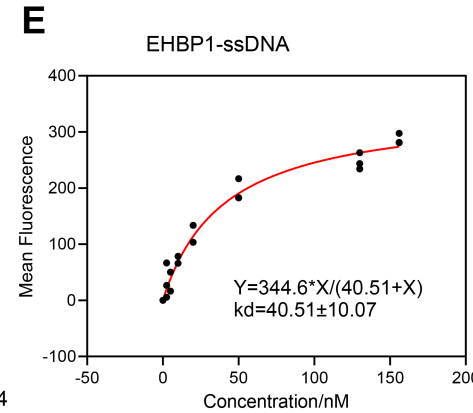

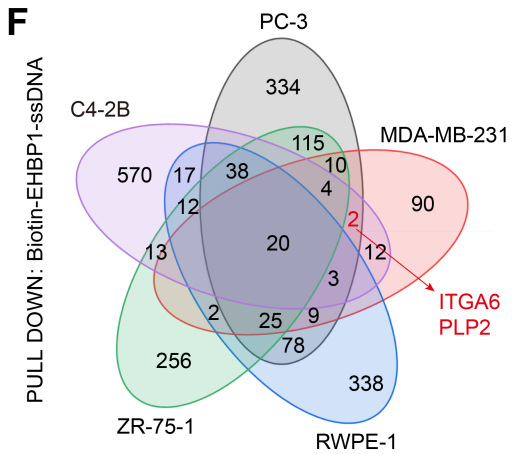

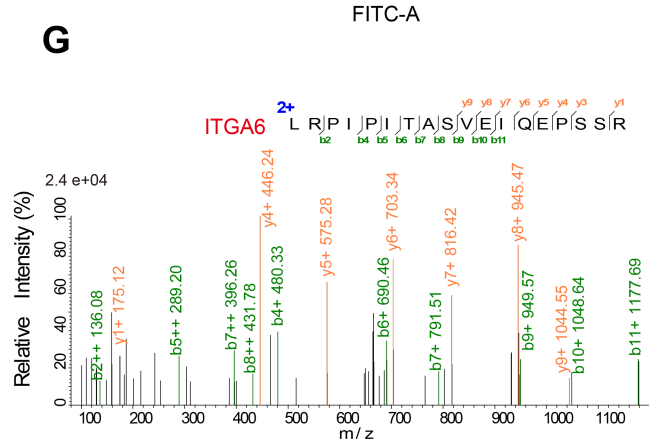

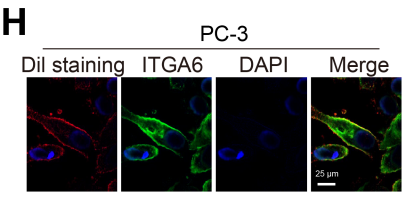

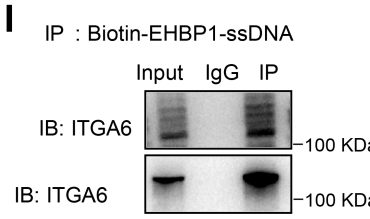

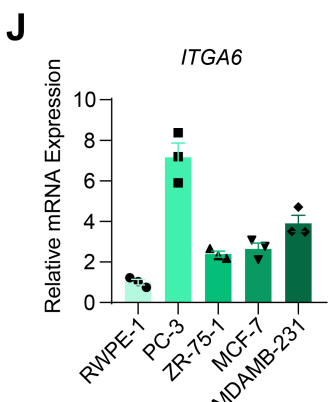

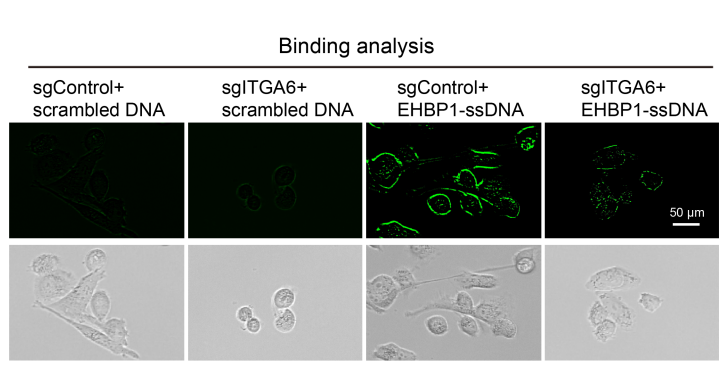

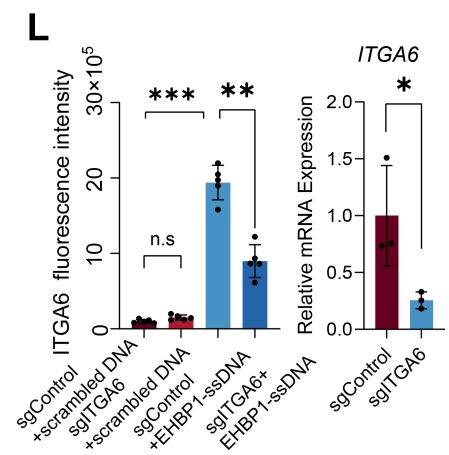

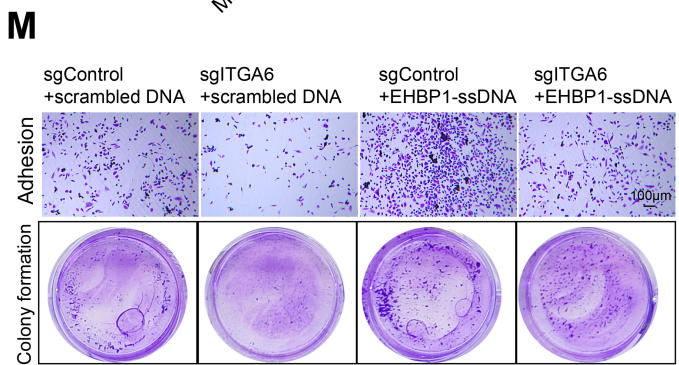

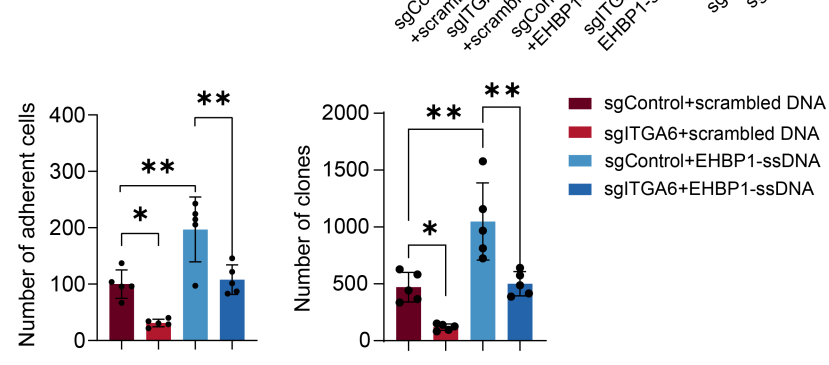

Figure 3

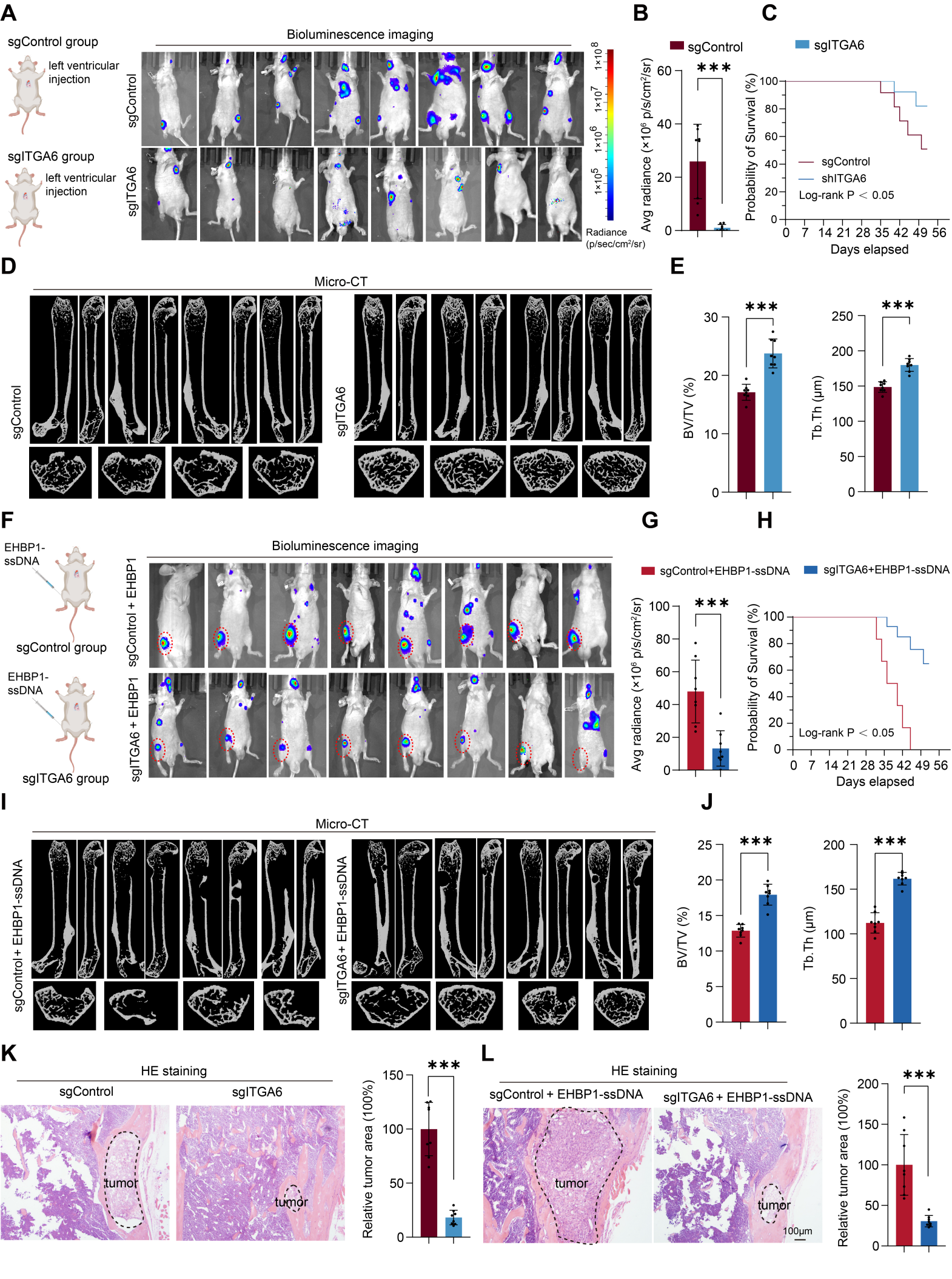
A
sgControl group
left ventricular injection
sgITGA6 group
left ventricular injection
Bioluminescence imaging
sgControl
sgITGA6
Radiance (p/sec/cm²/sr)
B
sgControl
sgITGA6
***
Avg radiance (×10⁶ p/s/cm²/sr)
C
Probability of Survival (%)
sgControl
shITGA6
Log-rank P < 0.05
Days elapsed
D
Micro-CT
sgControl
sgITGA6
E
***
BV/TV (%)
***
Tb.Th (μm)
F
EHBP1-ssDNA
sgControl group
EHBP1-ssDNA
sgITGA6 group
Bioluminescence imaging
sgControl + EHBP1
sgITGA6 + EHBP1
G
sgControl+EHBP1-ssDNA
sgITGA6+EHBP1-ssDNA
***
Avg radiance (×10⁶ p/s/cm²/sr)
H
Probability of Survival (%)
Log-rank P < 0.05
Days elapsed
I
Micro-CT
sgControl+ EHBP1-ssDNA
sgITGA6+ EHBP1-ssDNA
J
***
BV/TV (%)
***
Tb.Th (μm)
K
HE staining
sgControl
sgITGA6
tumor
tumor
***
Relative tumor area (100%)
L
HE staining
sgControl + EHBP1-ssDNA
sgITGA6 + EHBP1-ssDNA
tumor
tumor
100μm
***
Relative tumor area (100%)

Figure 4

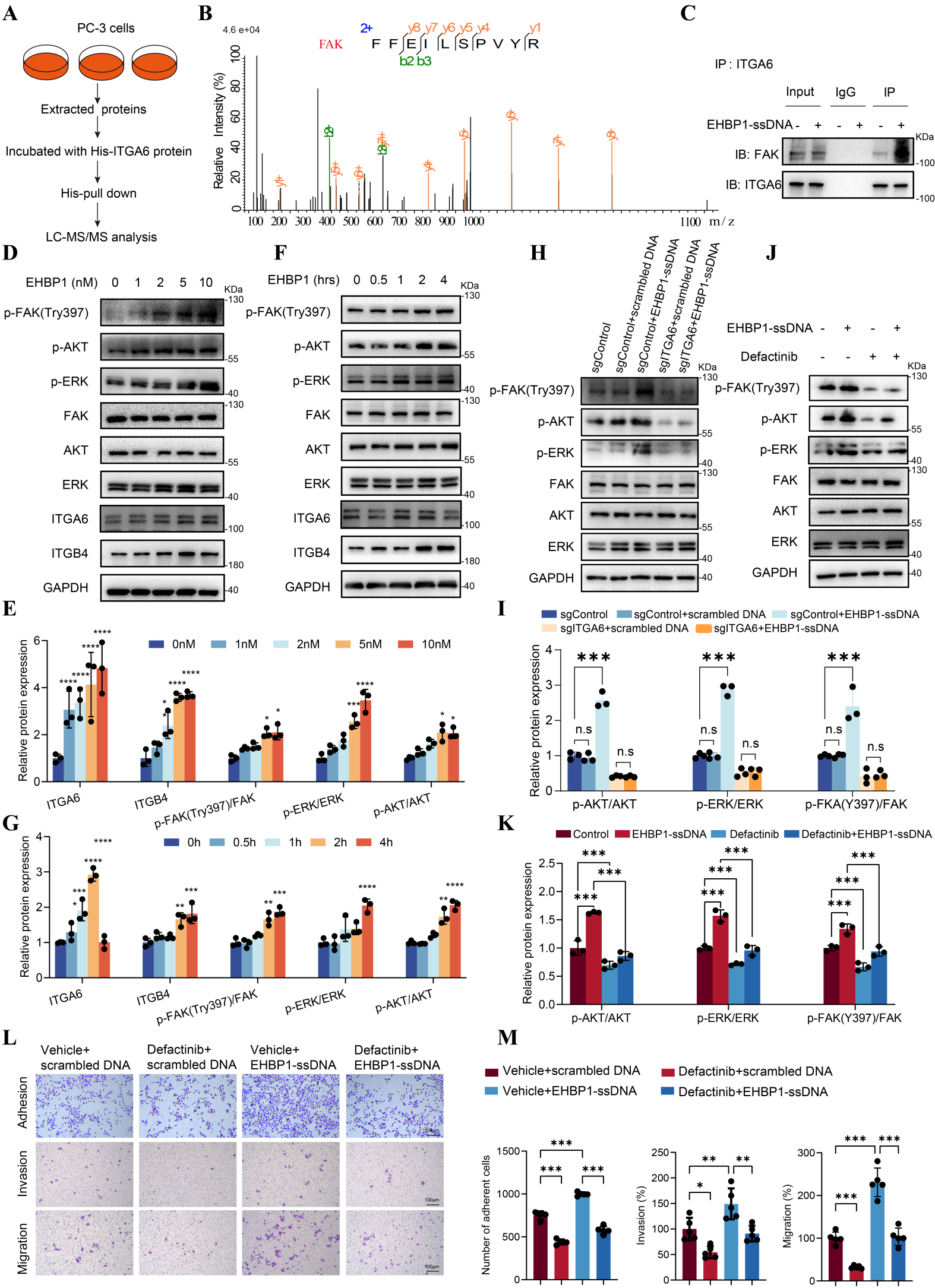
A
PC-3 cells
Extracted proteins
Incubated with His-ITGA6 protein
His-pull down
LC-MS/MS analysis
B
FAK
F F E I L S P V Y R
Relative Intensity (%)
m/z
C
IP : ITGA6
Input
IgG
IP
EHBP1-ssDNA
IB: FAK
IB: ITGA6
KDa
D
EHBP1 (nM) 0 1 2 5 10
p-FAK(Try397)
p-AKT
p-ERK
FAK
AKT
ERK
ITGA6
ITGB4
GAPDH
F
EHBP1 (hrs) 0 0.5 1 2 4
H
sgControl
sgControl+scrambled DNA
sgControl+EHBP1-ssDNA
sgITGA6+scrambled DNA
sgITGA6+EHBP1-ssDNA
J
EHBP1-ssDNA
Defactinib
E
0nM 1nM 2nM 5nM 10nM
Relative protein expression
ITGA6
ITGB4
p-FAK(Try397)/FAK
p-ERK/ERK
p-AKT/AKT
I
sgControl
sgControl+scrambled DNA
sgControl+EHBP1-ssDNA
sgITGA6+scrambled DNA
sgITGA6+EHBP1-ssDNA
n.s
p-AKT/AKT
p-ERK/ERK
p-FKA(Y397)/FAK
G
0h 0.5h 1h 2h 4h
K
Control
EHBP1-ssDNA
Defactinib
Defactinib+EHBP1-ssDNA
p-FAK(Y397)/FAK
L
Vehicle+ scrambled DNA
Defactinib+ scrambled DNA
Vehicle+ EHBP1-ssDNA
Defactinib+ EHBP1-ssDNA
Adhesion
Invasion
Migration
M
Vehicle+scrambled DNA
Defactinib+scrambled DNA
Vehicle+EHBP1-ssDNA
Defactinib+EHBP1-ssDNA
Number of adherent cells
Invasion (%)
Migration (%)

Figure 5

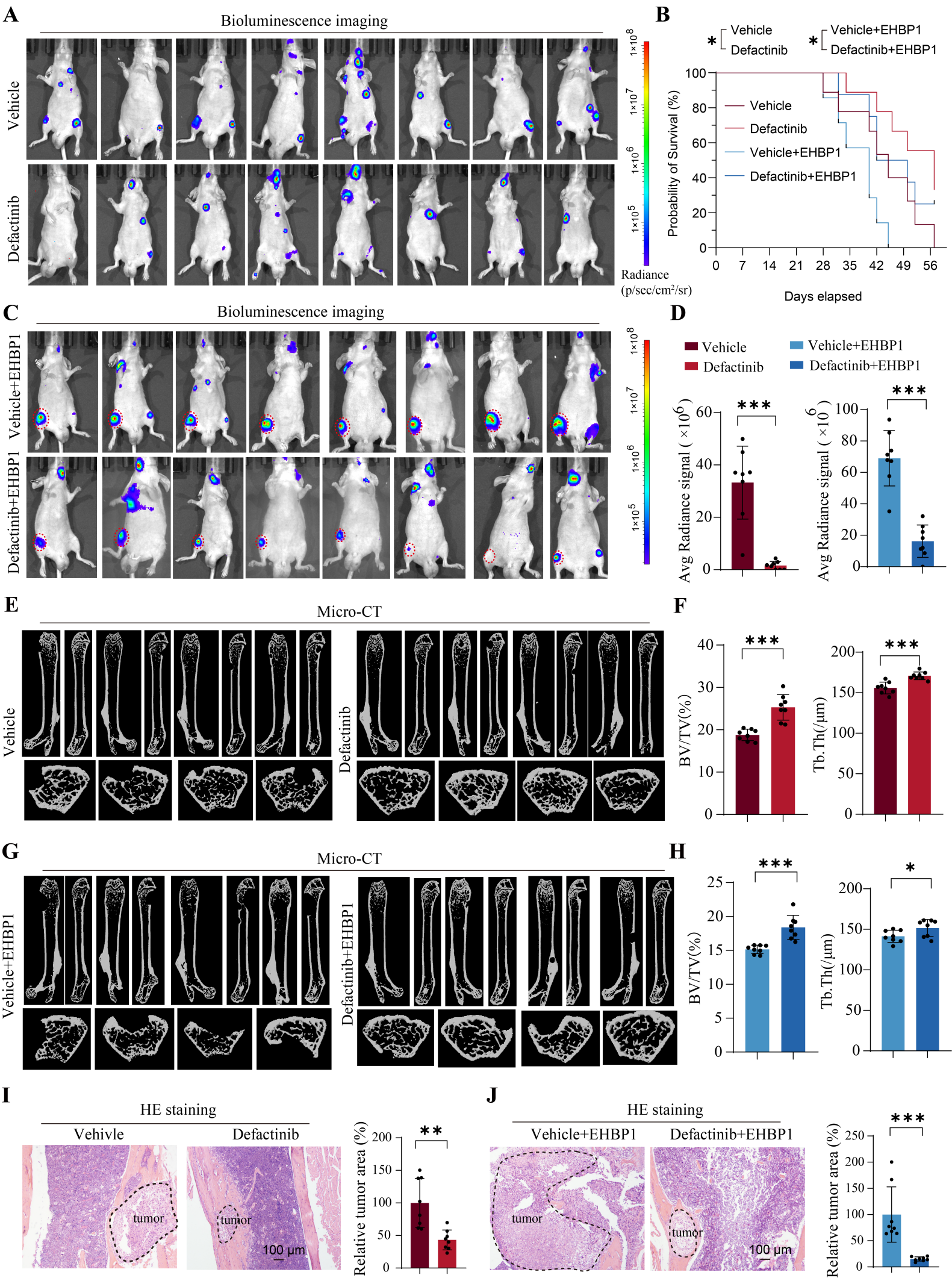
A
Bioluminescence imaging
Vehicle
Defactinib
Radiance (p/sec/cm²/sr)
B
Vehicle
Defactinib
Vehicle+EHBP1
Defactinib+EHBP1
Probability of Survival (%)
Days elapsed
C
Bioluminescence imaging
Vehicle+EHBP1
Defactinib+EHBP1
D
Avg Radiance signal (×10⁶)
Avg Radiance signal (×10⁶)
E
Micro-CT
Vehicle
Defactinib
F
BV/TV(%)
Tb.Th(/μm)
G
Micro-CT
Vehicle+EHBP1
Defactinib+EHBP1
H
BV/TV(%)
Tb.Th(/μm)
I
HE staining
Vehivle
Defactinib
tumor
100 μm
Relative tumor area (%)
J
HE staining
Vehicle+EHBP1
Defactinib+EHBP1
tumor
100 μm
Relative tumor area (%)

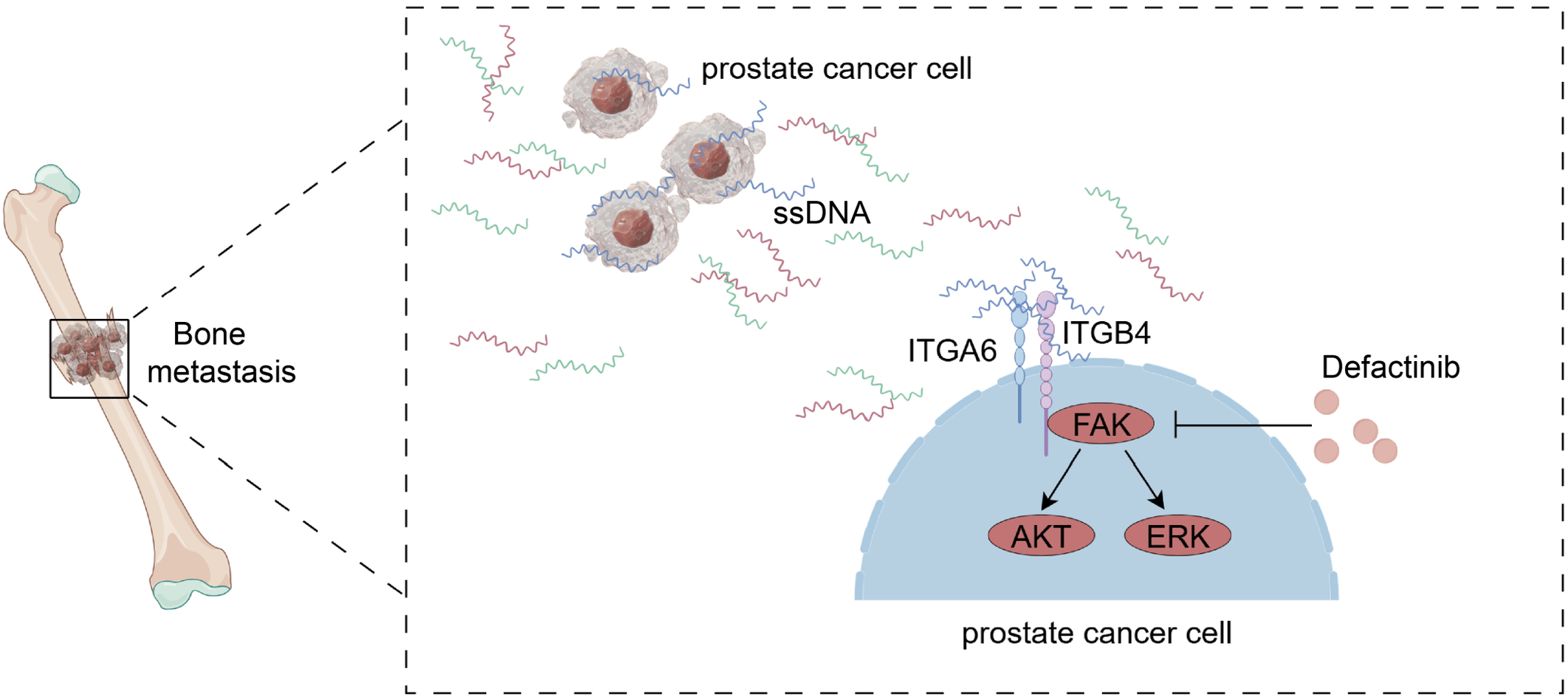
prostate cancer cell
ssDNA
Bone
metastasis
ITGA6
ITGB4
Defactinib
FAK
AKT
ERK
prostate cancer cell